



BAFFLES: Bayesian Ages for Field Lower-mass Stars

S. Adam Stanford-Moore¹ , Eric L. Nielsen^{1,2} , Robert J. De Rosa^{1,3} , Bruce Macintosh¹ , and Ian Czekala^{4,5} 

¹Kavli Institute for Particle Astrophysics and Cosmology, Stanford University, Stanford, CA 94305, USA; astanfordmoore@gmail.com

²Department of Astronomy, New Mexico State University, P.O. Box 30001, MSC 4500, Las Cruces, NM 88003, USA

³European Southern Observatory, Alonso de Córdova 3107, Vitacura, Santiago, Chile

⁴Department of Astronomy, 501 Campbell Hall, University of California, Berkeley, CA 94720-3411, USA

Received 2019 August 29; revised 2020 May 29; accepted 2020 June 4; published 2020 July 20

Abstract

Age is a fundamental parameter of stars, yet in many cases, ages of individual stars are presented without robust estimates of the uncertainty. We have developed a Bayesian framework, BAFFLES, to produce the age posterior for a star from its calcium emission strength ($\log(R'_{HK})$) or lithium abundance (Li EW) and $B - V$ color. We empirically determine the likelihood functions for calcium and lithium as functions of age from literature measurements of stars in benchmark clusters with well-determined ages. We use a uniform prior on age, which reflects a uniform star formation rate. The age posteriors we derive for several test cases are consistent with literature ages found from other methods. BAFFLES represents a robust method to determine the age posterior probability distribution for any field star with $0.45 \leq B - V \leq 0.9$ and a measurement of R'_{HK} and/or $0.35 \leq B - V \leq 1.9$ and measured Li EW. We compile colors, R'_{HK} , and Li EW from over 2630 nearby field stars from the literature, and present the derived BAFFLES age posterior for each star.

Unified Astronomy Thesaurus concepts: [Stellar activity \(1580\)](#); [Stellar ages \(1581\)](#); [Field stars \(2103\)](#); [Bayesian statistics \(1900\)](#)

Supporting material: machine-readable table

1. Introduction

Age, along with mass and metallicity, is a fundamental parameter of stars. Accurate stellar ages are needed in a wide variety of astronomical studies, including galactic evolution, globular clusters, open clusters, star-forming regions, stellar multiples, brown dwarf companions, and planetary systems. For direct imaging exoplanet surveys, such as the Gemini Planet Imager Exoplanet Survey (Macintosh et al. 2018; Nielsen et al. 2019), stellar age is important at all stages of the survey. First, while selecting target stars, younger stars are preferred, since their planets will be inherently brighter and easier to detect. Second, the mass for an imaged planet is derived from the age of the host star using evolutionary models that link mass, age, and luminosity (e.g., Allard 2014; Baraffe et al. 2015), and the dominant measurement uncertainty in deriving mass is from age (Bowler 2016). Third, age is a requirement for measuring the occurrence rates of planets. Translating sensitivity in apparent brightness to mass sensitivity requires the age of each observed star. Thus, completeness to planets as a function of mass, a key ingredient for occurrence rate, relies heavily on precise ages for the entire sample (e.g., Nielsen et al. 2013, 2019; Bowler 2016).

Ages of stars in coeval groups, such as open clusters or moving groups, are generally well-determined. Ages of field stars, however, are more difficult to determine robustly. For stellar clusters with well-determined membership lists, the main-sequence turnoff is used to robustly determine the age (e.g., Goudfrooij et al. 2014; Cummings & Kalirai 2018). The lithium depletion boundary (LDB) is applicable to both clusters and more sparse moving groups, with the reddest objects in an association with detectable lithium absorption setting the overall age (e.g., Burke et al. 2004; Soderblom 2010). For

isolated field stars, however, a less robust set of observables that track age are available, including spectroscopic indicators (e.g., Skumanich 1971; Wright et al. 2004), gyrochronology (e.g., Kraft 1967; Barnes 2009), and asteroseismology (e.g., Cunha et al. 2007). Here, we present a Bayesian method to determine age through two spectral indicators: calcium emission strength and the depth of the lithium absorption line.

1.1. Empirical Age Indicators

1.1.1. Calcium Emission Strength

Calcium emission strength, as given by the index R'_{HK} , is connected to the strength of a star's magnetic field through the stellar dynamo (Noyes et al. 1984). The rotation of the star and convection within induces a magnetic field whose strength is proportional to the rate of rotation (Skumanich 1971; Noyes et al. 1984). Over time, the star's rotation inevitably slows as it ejects ionized particles in its stellar wind, which carry away angular momentum (Kraft 1967; Weber & Davis 1967). As a result, the magnetic field strength—and thus, calcium emission strength—generally decrease with age.

The index R'_{HK} is a measure of the flux in the narrow emission line in the core of the Calcium II H and K absorption lines at $\sim 3968 \text{ \AA}$ and $\sim 3934 \text{ \AA}$, respectively (Noyes et al. 1984; Wright et al. 2004). Index R'_{HK} is derived from an intermediate index, the S index, which represents the ratio of the narrow emission flux to the background continuum flux. The S index provides a relative comparison of emission strength, yet includes both chromospheric and photospheric contributions and is dependent on $B - V$ (as well as age). Therefore, to remove the dependencies on $B - V$, the S index is transformed by two empirically determined polynomials in $B - V$, resulting in R'_{HK} (Noyes et al. 1984; Wright et al. 2004), where the polynomials have been calibrated over a $B - V$ range of 0.45–0.90, corresponding to an approximate spectral

⁵ NASA Hubble Fellowship Program Sagan Fellow.

type range of F6 to K2. In addition to the long-term decline in activity over time, the S value for a single star also varies by $\sim 10\%$ over that star’s activity cycle (Wright et al. 2004).

1.1.2. Lithium Equivalent Width (EW)

The strength of the lithium absorption line traces the amount of lithium present in the photosphere of a star. When stars initially form, their primordial lithium abundances are similar to the abundance from Big Bang nucleosynthesis, with number densities of $\sim 10^{-9}$ that of hydrogen (Sestito & Randich 2005). Over time, stars deplete their primordial lithium via nuclear burning in the core and convective mixing, such that measurements of remaining surface lithium correlate with stellar age (Skumanich 1971; Soderblom 2010). For stars cooler than ~ 7000 K, lithium abundance can be measured based on the EW of the absorption of the lithium doublet at 6708 \AA (Soderblom 2010); hotter stars (OBA spectral types) have ionized their lithium and have negligible 6708 \AA absorption even with no lithium burning.

Lithium’s two isotopes, ${}^6\text{Li}$ and the more abundant ${}^7\text{Li}$, burn at temperatures of 2.2 million K and 2.6 million K, respectively. Since stellar surface temperatures are much lower (~ 2500 K for low-mass M stars and $\sim 46,000$ K for high-mass O-stars), in order to burn, lithium must be brought into hotter layers via convection (Soderblom et al. 1990). As a result, the rate of lithium depletion largely depends on the depth of the convection zone, allowing lower-mass stars—which, while having lower surface temperatures, have much deeper convective layers—to deplete lithium faster than higher-mass stars (Soderblom et al. 1990). In addition to convection, it is thought that slow mixing induced by rotation and angular momentum loss may affect lithium depletion (Sestito & Randich 2005), such that lithium abundance is a function of age, spectral type, and the initial rotation rate and rotational evolution of the star.

1.2. Functional Fits to R'_{HK} and Li EW Evolution

Previous studies have taken advantage of the correlation between R'_{HK} and age to create empirical fits of mean cluster $\log(R'_{HK})$ versus \log cluster age (Soderblom et al. 1991; Donahue 1993; Lachaume et al. 1999; Mamajek & Hillenbrand 2008). However, while these polynomial fits allow one to find an expression for age as a function of R'_{HK} , the polynomial makes no direct prediction of uncertainty in the age derivation. Soderblom et al. (1991) found the standard deviation of their stellar data around their power-law fit to be ~ 0.2 dex and concluded that ages predicted from their fit would be accurate to $\sim 50\%$. A similar approach has been used for lithium as well (finding an average fit to clusters, and assigning a single age to a star based on its location relative to the cluster fits), e.g., in Mamajek et al. (2002) and Nielsen & Close (2010). However, this method fails to capture the full astrophysical scatter.

In addition, many polynomial fits fail to account for a uniform star formation rate in the Milky Way—with some exceptions, such as the second polynomial fit developed by Soderblom et al. (1991). Both Soderblom et al. (1991) and Mamajek & Hillenbrand (2008) note that using a one-to-one polynomial conversion between R'_{HK} and age on a volume-limited sample of solar-type stars results in an unphysically large number of stars with ages < 1 Gyr, compared to older stars, inconsistent with the expected local star formation history (their Figures 9 and 14, respectively). The polynomial fits

(e.g., Figure 2) tend to have slopes that become more negative when going to increasing age, such that the curve is flatter at small ages and steeper at larger ages. If scatter in R'_{HK} is symmetric (which we present evidence for in Section 3.1.4), this leads to a bias whereby systematically younger ages are predicted, because a 0.1 dex displacement toward more positive values of R'_{HK} moves along the flatter part of the curve to much younger ages, compared to an equal 0.1 dex displacement toward more negative values of R'_{HK} , which moves along the steeper part of the curve and does not move toward older ages as quickly. To illustrate this effect, we use the Mamajek & Hillenbrand (2008) polynomial giving $\log(\text{age})$ as a function of R'_{HK} (their Equation (3)). We generate 10^5 stars uniformly distributed in age between 1 Myr and 10 Gyr, then numerically invert the polynomial to assign a value of R'_{HK} to each, add 0.1 dex of Gaussian noise to each value, and use the polynomial to convert back to age. The returned age distribution has a significant spike at $\lesssim 1$ Gyr, which becomes more prominent as the amplitude of the Gaussian noise is increased. Soderblom et al. (1991) attempted to correct for this effect by adjusting the polynomial fit at large ages; they constrained it with the nearby star sample and assumed that sample had a uniform star formation rate. Mamajek & Hillenbrand (2008) advocate for an activity/rotation/age relation instead, which flattens out the age distribution of the volume-limited sample out to 6 Gyr. Here, we present an explicit prior uniform in age when creating age posterior probability density functions (PDFs) to address this issue.

Furthermore, the median age estimates for separate methods (e.g., R'_{HK} and Li EW) are difficult to rigorously combine without precise uncertainty estimates. Previous works have, for example, simply averaged the ages obtained from R'_{HK} and lithium (e.g., Nielsen & Close 2010).

Brandt et al. (2014a) developed a Bayesian method to combine the age PDF of a star’s likely moving group with its posterior PDF from indicators of chromospheric and X-ray activity and stellar rotation. The two age distributions are then averaged, weighted by the probability of membership to the moving group. Other works (e.g., Casagrande et al. 2011; Nielsen et al. 2013) have developed Bayesian methods for deriving age posteriors from isochrones that also utilize a uniform star formation rate prior.

We describe here a method to derive Bayesian ages for field stars from lithium or calcium measurements, Bayesian Ages For Field LowEr-mass Stars (BAFFLES).⁶ For calcium emission, our method is calibrated to stars with $B - V$ between 0.45 and 0.9 (\sim F6–K2) and $\log(R'_{HK})$ between -3.7 and -5 . For lithium, we have calibrated BAFFLES to stars with $B - V$ between 0.35 and 1.9 (\sim F2–M5) and Li EW between 3.2 and 1500 m\AA .

2. Data

We calibrate BAFFLES using benchmark moving groups and open clusters with well-determined ages. While calcium emission strength and lithium abundance serve as indicators of relative age, we use these clusters to calibrate the relationships that give age as a function of indicator. Table 1 gives basic

⁶ Our BAFFLES package is available at <https://github.com/adamstanfordmoore/BAFFLES> and can be used from the command line with `python baffles.py -bmv [B - V] -rhc [Log(R'_{HK})] -li [Li EW]` (with other options available). A static version of BAFFLES is available at doi:10.5281/zenodo.3840244.

Table 1
BAFFLES Benchmark Clusters for Both Calcium Emission and Lithium Abundance

Group Name	Age (Myr)	Age Reference	N_{Ca}	Ca Reference	N_{Li}	Li Reference
NGC 2264	5.5	(3)			123	(9), (10)
Upper Scorpius	10	(20)	8	(1)		
UCL+LCC	16	(21), (22)	8	(1)		
β Pic	24	(2)	6	(1), (30), (31)	37	(14), (19)
IC 2602	43.7	(4)			27	(11)
Tuc/Hor	45	(2)	6	(1), (32), (33)		
α Per	85	(1), (23), (24)	12	(1)	60	(15)
Pleiades	130	(1), (23), (25)	42	(1)	128	(6)
M35	200	(26)			82	(16)
M34	240	(5)			49	(12)
UMa	500	(27)	10	(1)		
Coma Ber	600	(13)			13	(17)
Hyades	700	(28), (34)	41	(1)	50	(7)
M67	4000	(29), (18)	70	(1)	40	(8)

Notes. N_{Ca} and N_{Li} refer to the number of stars from each cluster with literature calcium/lithium measurements.

References. (1) Mamajek & Hillenbrand 2008; (2) Bell et al. 2015; (3) Turner 2012; (4) Randich et al. 2018; (5) Meibom et al. 2011; (6) Soderblom et al. 1993; (7) Pace et al. 2012; (8) Jones et al. 1999; (9) Tobin et al. 2015; (10) King 1998; (11) Randich et al. 2001; (12) Jones et al. 1997; (13) King & Schuler 2005; (14) Mentuch et al. 2008; (15) Balachandran et al. 2011; (16) Anthony-Twarog et al. 2018; (17) Ford et al. 2001; (18) Vandenberg & Stetson 2004; (19) Shkolnik et al. 2017; (20) Pecaut & Mamajek 2016; (21) Mamajek et al. 2002; (22) de Zeeuw et al. 1999; (23) Barrado y Navascués et al. 2004; (24) Makarov 2006; (25) Duncan et al. 1991; (26) Sung & Bessell 1999; (27) King et al. 2003; (28) Brandt & Huang 2015; (29) Giampapa et al. 2006; (30) Wright et al. 2004; (31) Gray et al. 2006; (32) Jenkins et al. 2006; (33) Henry et al. 1996; (34) Gossage et al. 2018.

properties on each benchmark cluster as well as our assumed age for each.

Since the ages of the benchmark clusters anchor the calcium and lithium age relations, accurate ages are important to the accuracy of BAFFLES; the offset in the posteriors scales with the factor by which the ages are modified. For both lithium and calcium, modifying the age of a single cluster by $\pm 1\sigma$, tends to change the median age derived by BAFFLES by $\lesssim 3\%$. Systematically shifting all the cluster ages in the same direction by $\pm 1\sigma$ shifts the derived median ages of posteriors by a comparable amount, $\lesssim 20\%$.

2.1. Calcium Benchmark Clusters

Ages, stellar R'_{HK} values, and stellar $B - V$ values used in this work for calcium were compiled by Mamajek & Hillenbrand (2008), but here separately reported measurements for the same star are averaged together (though this had little effect on our fits). Adopted ages for the benchmark clusters were mostly identical to those adopted by Mamajek & Hillenbrand (2008), except we used more recent age estimates of 24 Myr for β Pic and 45 Myr for Tuc/Hor from Bell et al. (2015), 10 Myr for Upper Scorpius from Pecaut & Mamajek (2016), and ~ 700 Myr for Hyades from Brandt & Huang (2015) and Gossage et al. (2018).

2.2. Lithium Benchmark Clusters

We compiled $B - V$ and Li EW measurements from the multiple sources listed in Table 1. We averaged measurements for duplicate stars, and used the measurement if there was one measurement and one upper limit.

We used the stellar $B - V$ values if they were provided for individual stars; otherwise, we used $B - V$ magnitudes compiled from the literature in Table A1, which are all in nearby moving groups with negligible reddening. For stars in clusters with significant reddening, we converted spectral type or T_{eff} to $B - V$. Soderblom et al. (1993) (Pleiades), Jones et al. (1997)

(M34), and Jones et al. (1999) (M67) reported dereddened $(B - V)_0$, while Randich et al. (2001) (IC 2602), Anthony-Twarog et al. (2018) (M35), Ford et al. (2001) (Coma Ber), and Pace et al. (2012) (Hyades) gave uncorrected $B - V$. NGC 2264 lithium EWs from Tobin et al. (2015) were not accompanied by $B - V$ values, so we converted spectral type to $B - V$ using the conversion in Pecaut & Mamajek (2013). For α Per (Balachandran et al. 2011), we converted T_{eff} (which had been inferred from $V - K$ color) to $B - V$ also using the conversion in Pecaut & Mamajek (2013). For β Pic (Mentuch et al. 2008; Shkolnik et al. 2017), a moving group $\lesssim 100$ pc, we expect negligible reddening, and we took the observed $B - V$ colors (given in Table A1) to be the intrinsic colors.

Close binaries present an issue since it is not always clear whether the B magnitude, V magnitude, or lithium absorption are resolved or from the combined systems. To avoid this issue, for β Pic moving group members we removed the following binaries from Mentuch et al. (2008): AZ Cap, CD-64 1208, GJ 3305, AT Mic A, AT Mic B, HIP 23418, LP 476-207. We also removed binaries from Shkolnik et al. (2017): PM J01071-1935, LP 467-16, Barta 161 12, BD+17 232, CD-44 753, PM J05243-1601, GSC 06513-00291, MCC 124, TWA 22, CD-64 1208, AT Mic, GR* 9. We also removed stars with poorly measured values of B or V magnitudes (uncertainty $\gtrsim 0.15$ mag) from Mentuch et al. (2008): HD 164249B. The same was done for the following stars from Shkolnik et al. (2017): FK Psc, BD +30 397, EXO 0235.2-5216, 2MASS J05200029+0613036, RX J0520.5+0616, Smethells 20, CD-31 16041, TYC 6872-1011-1, TYC 7443-1102-1, BD-13 6424, UCAC4 396-055485.

For M67, we removed stars identified by Jones et al. (1999) as being less secure members, as well as potentially unresolved binaries. In many cases, Li EW is given without measurement error, with the exceptions of Mentuch et al. (2008) and Randich et al. (2001), which did provide individual errors. For Coma Ber, we also omitted stars that Ford et al. (2001) identified as nonmembers or spectroscopic binaries.

3. Methods

BAFFLES is a Bayesian framework that finds a star's posterior age PDF from input of R'_{HK} , or $B - V$ combined with Li EW, or all three. We calibrate the method using data sets of the benchmark clusters discussed above.

3.1. Calcium

Using the cluster data, we first present an age posterior from an R'_{HK} measurement of calcium emission.

3.1.1. Framework

We seek an expression that returns an age PDF for a single star given an R'_{HK} measurement, which is the posterior

$$p(t|\hat{r}), \quad (1)$$

where t is the age and \hat{r} is the measured value of R'_{HK} for a single star, with measurement uncertainty of $\sigma_{\hat{r}}$. We evaluate this posterior using Bayes' rule

$$p(\theta|D) = \frac{1}{Z} p(D|\theta) p(\theta), \quad (2)$$

where the four terms are posterior ($p(\theta|D)$), evidence (Z), likelihood ($p(D|\theta)$), and prior ($p(\theta)$), functions of the data (D) and parameters of the model (θ).

For calcium, the parameters of our model, θ , are the age t and the true value of R'_{HK} for the star, r , while the data, D , are our measured value of R'_{HK} , \hat{r} . We also assume the evidence, Z , is a constant. With these terms, Bayes' rule becomes

$$p(r, t|\hat{r}) \propto p(\hat{r}|r, t) p(r, t). \quad (3)$$

Our knowledge of the true value of R'_{HK} for the star, r , comes from a measurement with an associated measurement error: \hat{r} and $\sigma_{\hat{r}}$. In the case of R'_{HK} , the astrophysical scatter among stars in a single cluster is generally much larger than the measurement uncertainty for any one star. Thus, our model should incorporate both the overall trend that, for clusters of different ages, average r (μ_r) decreases with increasing age, and that there is a scatter about this mean at a single age (σ_r). We expect both these terms to evolve with time, and express them as functions $\mu_r = f(t)$ and $\sigma_r = g(t)$. If the scatter is fit by a Gaussian, our prior on r then becomes

$$p(r|t) = \mathcal{N}(r|f(t), g(t)), \quad (4)$$

while the prior on t , $p(t)$, is flat for a uniform star formation rate, uniform in linear age between 1 Myr and 13 Gyr. Although the star formation rate increases at ages older than ~ 8 Gyr, this prior is a reasonable approximation for ages < 5 Gyr (Snaith et al. 2015), which also corresponds to the oldest benchmark clusters we utilize. Higher-mass stars have main-sequence lifetimes shorter than the full range of our prior. A stellar lifetime prior is a complicated function of $B - V$, especially because stars of a given mass evolve in color over time. Rather than commit to a particular set of isochrones, we choose to keep BAFFLES as empirically driven as possible. An isochrone-based age prior can be applied to a BAFFLES posterior once generated, and we advise caution when considering an age posterior with significant probability at very large ages for higher-mass stars. Together, these define a

joint prior for our problem

$$p(r, t) = p(r|t)p(t) = \mathcal{N}(r|f(t), g(t))p(t). \quad (5)$$

In the general case of measurements with Gaussian error bars, likelihood would be given by a normal distribution,

$$\mathcal{L}(\hat{r}|r) = \mathcal{N}(\hat{r}|r, \sigma_{\hat{r}}). \quad (6)$$

However, for R'_{HK} , we assume that the uncertainty is negligible, especially given the larger astrophysical scatter, σ_r . Therefore, we instead take the likelihood to be a delta function,

$$p(\hat{r}|r) = \mathcal{L}(\hat{r}|r) = \delta(r - \hat{r}). \quad (7)$$

We have no direct data on the age, t , but it is a parameter of our model, so we rewrite the likelihood as

$$p(\hat{r}|r) = p(\hat{r}|r, t) = \delta(r - \hat{r}). \quad (8)$$

We can now rewrite Equation (8), the joint posterior over r and t , as

$$p(r, t|\hat{r}) \propto \delta(r - \hat{r}) \mathcal{N}(r|f(t), g(t)) p(t), \quad (9)$$

and after marginalizing over r and taking $p(t)$ to be a constant, we solve for $p(t|\hat{r})$,

$$p(t|\hat{r}) \propto \int p(r, t|\hat{r}) dr = \mathcal{N}(r|f(t), g(t)). \quad (10)$$

If the astrophysical scatter is Gaussian, then by determining functional forms for $f(t)$ and $g(t)$ from our cluster data, we can evaluate the likelihood and produce a posterior for any star given a measurement \hat{r} . In Section 3.1.4, however, we present evidence that the scatter is not well-modeled by a Gaussian, and introduce a new numerical function to describe the prior on r .

3.1.2. The Color Dependence of R'_{HK}

The derived quantity R'_{HK} is formulated to be independent of $B - V$ color, which is accomplished by using two polynomials in $B - V$ to convert the raw S_{HK} value into R'_{HK} . To determine the extent to which R'_{HK} is in fact independent of color, we initially considered using a two-parameter linear fit to the cluster R'_{HK} as a function of $B - V$, similar to that in Mamajek & Hillenbrand (2008), since the slopes seemed non-negligible. However, since our data set included many clusters with only a handful of calcium measurements, the fit slopes were poorly determined and the fits crossed frequently, the latter being a nonphysical outcome. As in the right panel of Figure 1, linear fits to the clusters resulted in nonmonotonic changes in R'_{HK} over time, especially in the reddest and bluest regions of our $B - V$ range. Although Mamajek & Hillenbrand (2008) used linear fits for each cluster, they interpolated cluster means for solar $B - V$ (~ 0.65) only. For solar $B - V$, the cluster means are still monotonic, something not true for other $B - V$ values that were included in our study.

There is a significant improvement in χ^2 from the linear fit to the constant fit, dropping from 554 (constant) to 423 (linear), assuming a constant measurement error for each star of 0.1 dex, as estimated by Mamajek & Hillenbrand (2008). Based on the Bayesian information criterion, this presents very strong evidence in favor of the linear model ($\Delta\text{BIC} = 83.3$). Nevertheless, we find the behavior of the linear fits in the right panel of Figure 1 to be unphysical: at the reddest and bluest ends, the evolution in R'_{HK} is nonmonotonic and implies wild swings in

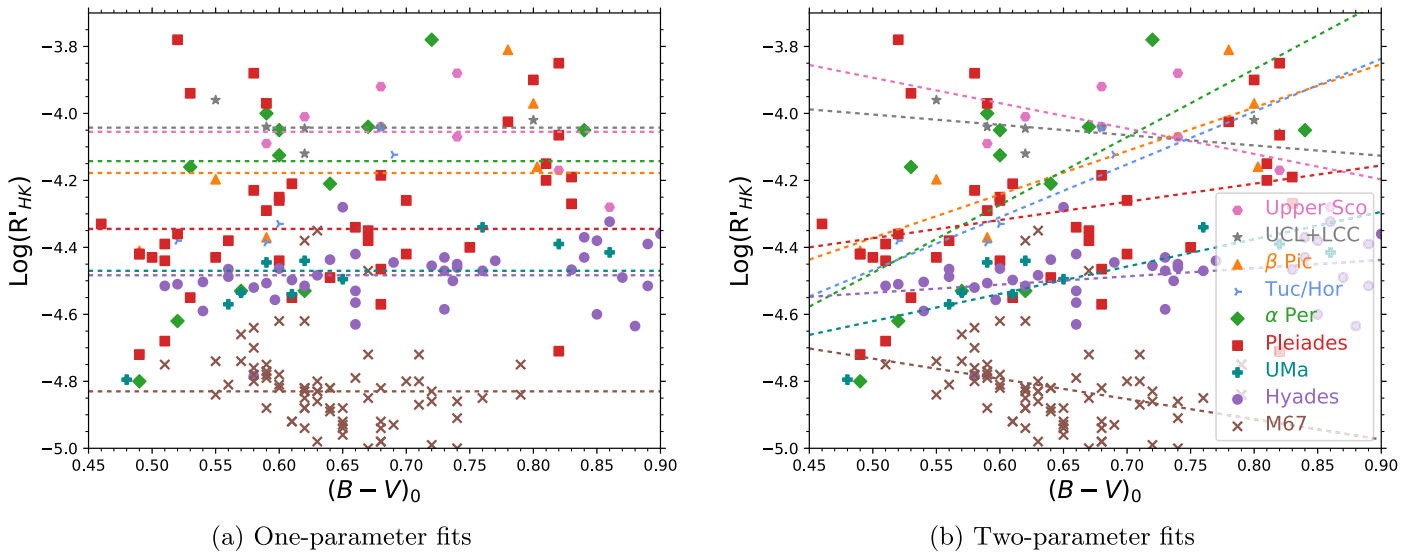


Figure 1. Left: one-parameter fits with no color dependence avoid overfitting. Right: linear fits to the $B - V$ dependence of R'_{HK} for each cluster are dominated by outliers for sparse data sets, and become nonmonotonic at the blue and red ends. We adopt the one-parameter fit in the final prior function $f(t)$.

calcium activity as a function of age, based on a handful of data points in each cluster, as well as poor sampling across the entire $B - V$ range. As a result, to avoid overfitting sparse data, we adopted a constant fit for R'_{HK} , where each cluster is represented by the median value of R'_{HK} , with no $B - V$ dependence. A constant fit has the advantage of capturing the monotonic decrease in R'_{HK} while remaining the simplest fit. Mamajek & Hillenbrand (2008) advocate determining age from R'_{HK} through an age–activity–rotation relation, the effect of which is a significant $B - V$ dependence on R'_{HK} for objects of similar ages (see their Figure 11), which varies by ~ 0.15 dex across $B - V$. As there are limited R'_{HK} measurements in benchmark clusters, it is currently difficult to confirm this behavior of R'_{HK} as a function of color. In fact, more direct solutions to a $B - V$ dependence of R'_{HK} would be to either redetermine the polynomial parameters or to fit directly in S_{HK} , and either would likely require a larger data set than that presented here.

3.1.3. R'_{HK} as a Function of Age

From the fits above, we have nine cluster ages and their respective mean $\log(R'_{HK})$ values, which we use to find the mean $\log(R'_{HK})$ at all ages covered by our prior, $\mu_r = f(t)$. We fit $\log(R'_{HK})$ as a function of age with a second-order polynomial, constrained to be monotonically decreasing, and where each cluster in the fit is weighted by the number of stars it contains. Figure 2 shows this fit against the median value of each cluster, with plotted error bars indicating the standard deviation in each cluster. Our fit is consistent with polynomial fits from previous authors. Mamajek & Hillenbrand (2008) use linear fits for finding each cluster’s mean R'_{HK} as a function of $B - V$, and then fit a third-order polynomial to age, based on the value of each cluster’s linear fit evaluated at solar $B - V$ of 0.65. The largest discrepancies between the two fits are, unsurprisingly, at ages lower than that of the youngest benchmark cluster (Upper Sco) and larger than that of the oldest (M67). Soderblom et al. (1991) experimented with several different second-order polynomials, correcting for disk heating and a uniform star formation rate.

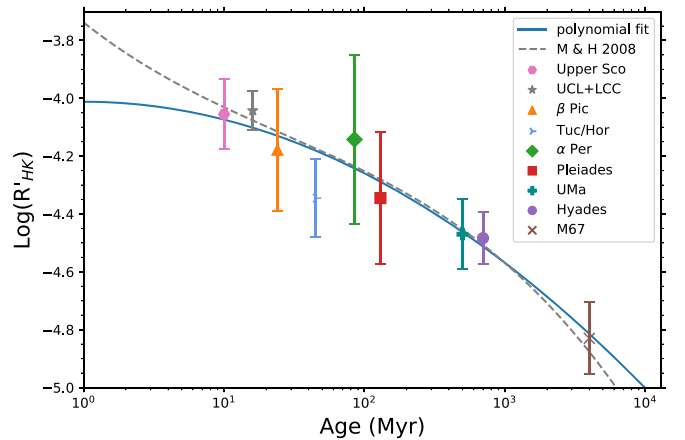


Figure 2. Fit for the mean R'_{HK} as a function of age using cluster median values. Error bars on each point represent the standard deviation of $\log(R'_{HK})$ in each cluster, while the fit is weighted only by the number of points in each cluster. Observed variation is consistent with R'_{HK} decreasing monotonically with time. Solid blue line is our second-order polynomial fit to cluster median activity, which is very similar to the overplotted third-order polynomial (gray dashed line) from Mamajek & Hillenbrand (2008), based on a nearly identical data set.

3.1.4. Astrophysical Scatter

We next examine the astrophysical scatter of R'_{HK} about the mean, $\sigma_r = g(t)$. We begin by computing the residuals of R'_{HK} for every star in a cluster to the median value for all stars in the cluster. The standard deviations of these residuals are plotted in Figure 3, where uncertainty in the standard deviation (σ_m) of the m th cluster with N_m stars is given by the equation appropriate for Gaussian scatter, $\pm \frac{\sigma_m}{\sqrt{2N_m - 2}}$. There is some evidence that the scatter between 20 and 200 Myr is larger than the scatter for younger or older stars. This is reminiscent of Figure 1 of Gallet & Bouvier (2013), where solar-type stars spin up between ~ 10 and 50 Myr as they contract when approaching the main sequence, and the dispersion in rotation rate between the fast rotators and slow rotators in a single cluster increases, compared to stars younger than 20 Myr or older than 200 Myr. We investigated using a Gaussian or

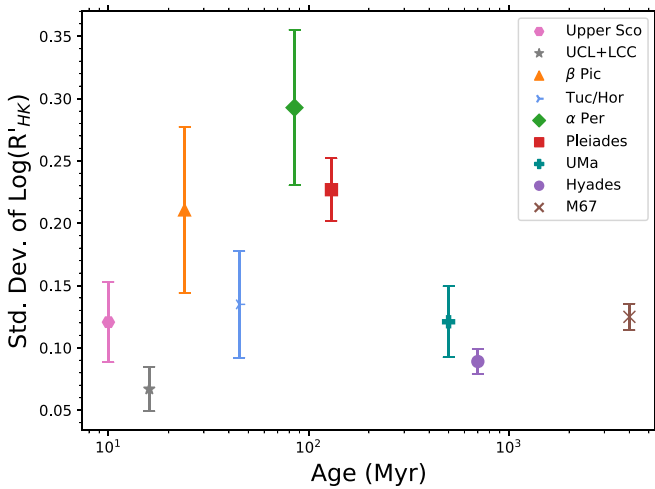


Figure 3. Standard deviations of the residuals to the median of each calcium cluster, along with computed uncertainties. Scatter in R'_{HK} over time appears to increase between 20 and 200 Myr, suggestive of a similar effect in the scatter of rotation rate as a function of age (Gallet & Bouvier 2013). The three clusters with the most measurements, Pleiades, Hyades, and M67, show a significant offset at ~ 100 Myr (compared to >700 Myr). Many of the remaining clusters, however, have fewer than 10 stars with calcium measurements, and as such, they poorly determine the standard deviation. More measurements of stars in these young clusters are needed in order to robustly map out any age dependence.

inverted parabola to fit the data, but we do not have strong evidence that such a fit is justified. The clusters with the most measurements, Pleiades, Hyades, and M67, show the strongest evidence for a change in the standard deviation with time. However, the clusters Upper Sco, UCL+LCC, β Pic, Tuc/Hor, α Per, each have only a few stars (8, 8, 6, 6, and 12 respectively), meaning the standard deviations are not well-determined. As a result, we treat $g(t)$ as a constant and note that larger data sets with more stars in these young clusters would be needed in order to precisely measure time-dependent behavior.

We instead compute the residuals for each star with respect to the fit $f(t)$, and observe that these residuals, while somewhat symmetric, are not well-fit by a Gaussian (the dashed gray curve in Figure 4). In particular, the best-fit Gaussian underestimates the peak and is significantly wider at $\sim 1\sigma$ compared to the data. We thus return to Equation (4) and replace the normal distribution in our prior with a new numerical function,

$$p(r|t) = \mathcal{H}(r|f(t)), \quad (11)$$

which has a mean $f(t)$. The amplitude of the scatter is encoded by \mathcal{H} itself, and since we take $g(t)$ to be a constant, the shape of \mathcal{H} does not change over time, only its mean.

To evaluate \mathcal{H} , we fit a function to the smoothed CDF of the residuals, as in the right panel of Figure 4, capturing the non-Gaussian shape of the astrophysical scatter. The tails of the PDF are constrained to decrease exponentially out to ~ 4 standard deviations and then are fixed at zero. We perform the smoothing with a Savitzky–Golay filter, which fits successive windows with a third-order polynomial so as to remove jumps in the function from star to star without significantly increasing the width of the distribution. The final function is a good fit to the data (see left panel of Figure 4). We normalize the final \mathcal{H} distribution so that it has an integral of unity. Then, since we

find \mathcal{H} to be slightly asymmetric with a median of 0.0026 dex, we shift the distribution so that its median has a value of zero.

The numerical fit \mathcal{H} is one of many possible implementations of the prior function. Other choices with wider tails (such as the Student’s-t distribution or the Lorentzian distribution) also partially capture the non-Gaussian behavior. We found the best fit with the Student’s-t distribution, which came closest to matching the residual distribution. We also found no significant difference between it and the empirical function \mathcal{H} on our final age posteriors.

3.1.5. Calcium Posterior

Rewriting Equation (8), we then have an expression for our posterior given by

$$p(r, t|\hat{r}) \propto \delta(r - \hat{r})\mathcal{H}(r|f(t))p(t), \quad (12)$$

where f and \mathcal{H} are determined from our cluster data sets above, and $p(t)$ is constant for a uniform star formation rate. We can then rewrite our calcium age posterior in Equation (10) using our function \mathcal{H} :

$$p(t|\hat{r}) \propto \mathcal{H}(\hat{r}|f(t)). \quad (13)$$

We implement this method with an array of 1000 elements uniformly sampled in log age from 1–13,000 Myr, and we evaluate Equation (13) at each point in the array for the \hat{r} of a single star. These probabilities are then normalized to integrate to unity (accounting for uneven bin sizes) and provide the age posterior for that star.

3.2. Lithium

Overall, we follow the same procedure for lithium as for calcium, with two major differences: lithium depletion has a strong $B - V$ color dependence (unlike the R'_{HK} metric for calcium, which was specifically formulated to be independent of color), and lithium measurements can have significant error bars or upper limits.

3.2.1. Framework

As with calcium, lithium EW decreases with time, with an astrophysical scatter about this trend for objects of the same age. Following the framework we developed for calcium, we define functions for the mean EW as a function of time (i), the standard deviation about that mean (j), and the shape of the distribution function about the mean (\mathcal{K}). These three functions are the lithium equivalents of f , g , and \mathcal{H} used above for calcium. The mean $i(t, b)$ is decidedly a function of both age (t) and $B - V$ color (b). However, when we consider the log of the EW (l), the scatter about this mean appears to be independent of color, so we define $j(t)$ as a function of time only. The parameters of our model are l , b , and t , requiring a joint prior in all three for Bayes’ equation, $p(l, b, t)$,

$$p(l, b, t) = p(l|b, t)p(b)p(t) = \mathcal{K}(l|i(t, b), j(t))p(b)p(t), \quad (14)$$

where $p(b)$ is the prior on $B - V$ color, which we take to be flat, since we will generally have a precise measurement of color for a given star, and $p(t)$ is the prior on age, again flat for a constant star formation rate.

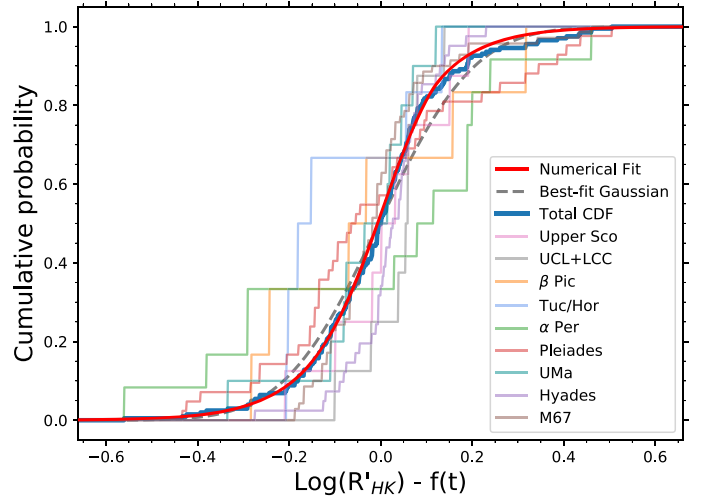
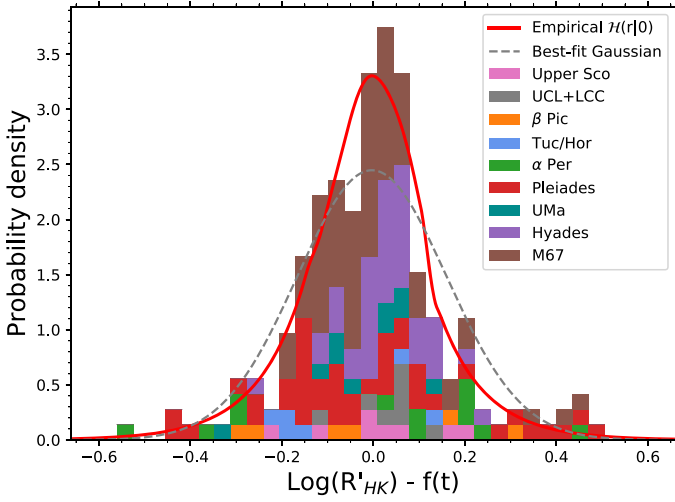


Figure 4. Left: histogram of residuals of all cluster stars to the fit $f(t)$. Distribution appears significantly non-Gaussian, as the best-fit Gaussian (dashed gray line) has a lower peak and overpredicts the number of stars at $\sim 1\sigma$. Instead, we construct a numerically determined function from our data (red line, $\mathcal{H}(r|f(t))$). Right: CDF of the residuals, from which we construct the empirical function \mathcal{H} .

We assume a Gaussian likelihood for both l and b , given measurements of \hat{l} and \hat{b} , and measurement errors of σ_l and σ_b ,

$$\mathcal{L}(\hat{l}, \hat{b}) = \mathcal{N}(10^{\hat{l}}|10^l, \sigma_l)\mathcal{N}(\hat{b}|b, \sigma_b), \quad (15)$$

where 10 is raised to the power of l and \hat{l} because, while l is a log quantity, measurement errors are typically quoted in linear units (e.g., mÅ). Combining likelihood and prior, and again assuming the evidence to be constant, we obtain an expression for the posterior

$$p(l, b, t|\hat{l}, \hat{b}) \propto \mathcal{N}(10^{\hat{l}}|10^l, \sigma_l)\mathcal{N}(\hat{b}|b, \sigma_b)\mathcal{K}(l|i(t, b), j(t)), \quad (16)$$

which, when marginalized over l and b , gives the marginalized posterior on age,

$$p(t|\hat{l}, \hat{b}) = \int \int p(l, b, t|\hat{l}, \hat{b}) dl db. \quad (17)$$

As with calcium, all that remains is to define the functions $i(t, b)$, $j(t)$, and $\mathcal{K}(l|i(t, b), j(t))$ from our cluster data.

3.2.2. The Color Dependence of Li EW

For a single cluster, the log of the EW, l , appears as a Gaussian or parabola as a function of $B - V$, as shown in Figure 5. The reddest and bluest stars in the cluster tend to have the smallest values for lithium EW, while intermediate $B - V$ stars (G stars) have the largest lithium EW. This behavior is the result of two primary processes. First, redder, lower-mass stars have deeper convective envelopes, so they more quickly convect lithium to deeper, hotter layers of the star, where it is fused, resulting in faster depletion of lithium. Meanwhile, blue stars have hotter photospheres, so there are fewer lithium atoms in the ground state to absorb 6708 Å light. Stars are expected to have uniform lithium abundance ($N(\text{Li})$) at formation, but this translates to a range of Li EW values as a function of color, given the different photospheric temperatures across this range. In addition to the Gaussian shape, the “lithium dip” is observed for stars between $B - V$ of ~ 0.36 and ~ 0.42 (6900 K and 6600 K) for stars that are $\gtrsim 500$ Myr, where there is a decrease in lithium abundance in this narrow range compared to stars on either side of the dip (Boesgaard & Tripicco 1986;

Balachandran 1995). A suggested explanation for the lithium dip is that, at the hot end of the dip, magnetic field strength is increasing with decreasing stellar mass, spinning down the outer layers of the star and creating turbulent mixing from internal shear between these layers and the faster-rotating core. Moving to the cooler end of the dip thus corresponds to the rise of internal gravity waves, which more efficiently spin down the core, such that there is less turbulent mixing (Talon & Charbonnel 2010). Under this model, surface lithium is preferentially destroyed in the narrow region of the lithium dip, while it is preserved on either side.

For each cluster, we simultaneously fit both the mean and the standard deviation of l at a single value of $t = t_m$, where t_m is the age of the given cluster m . We take these fits, $i'(t_m, b)$ and $j'(t_m)$, as preliminary values for the mean, $i(t, b)$, and standard deviation, $j(t)$, evaluated at the age of the cluster. We assume a functional form of a second-order polynomial for $i'(t_m, b)$, while at a single age the standard deviation, $j'(t_m)$, is a constant that does not depend on color. To fit these parameters, we assumed a Gaussian likelihood, which for lithium detections takes the form

$$p(\hat{l}|t_m, b) = \mathcal{N}(\hat{l}|l, \sigma_l) = \frac{1}{\sqrt{2\pi}j'(t_m)} e^{-\frac{(\hat{l}-i'(t_m, b))^2}{2j'(t_m)^2}}. \quad (18)$$

For lithium upper limits (\hat{u}), we represent the likelihood as the integral of the Gaussian function from $-\infty$ to the upper limit \hat{u} ,

$$p(\hat{u}|t_m, b) = \int_{-\infty}^{\hat{u}} \frac{1}{\sqrt{2\pi}j'(t_m)} e^{-\frac{(l-i'(t_m, b))^2}{2j'(t_m)^2}} dl, \quad (19)$$

and then fit these four parameters—three for the polynomial in b that defines $i'(t_m, b)$, and one for the standard deviation, $j'(t_m)$. The fit itself is performed by assigning one of these likelihoods to each star, based on whether there is a lithium measurement or upper limit, then maximizing the product of likelihoods over all cluster stars.

The lithium dip is clear in the ~ 700 Myr Hyades data set, so we fit an inverted Gaussian to the dip ($0.39 < B - V < 0.52$) and a second-order polynomial to the stars outside the dip. There is no clear evidence for a lithium dip at younger ages in

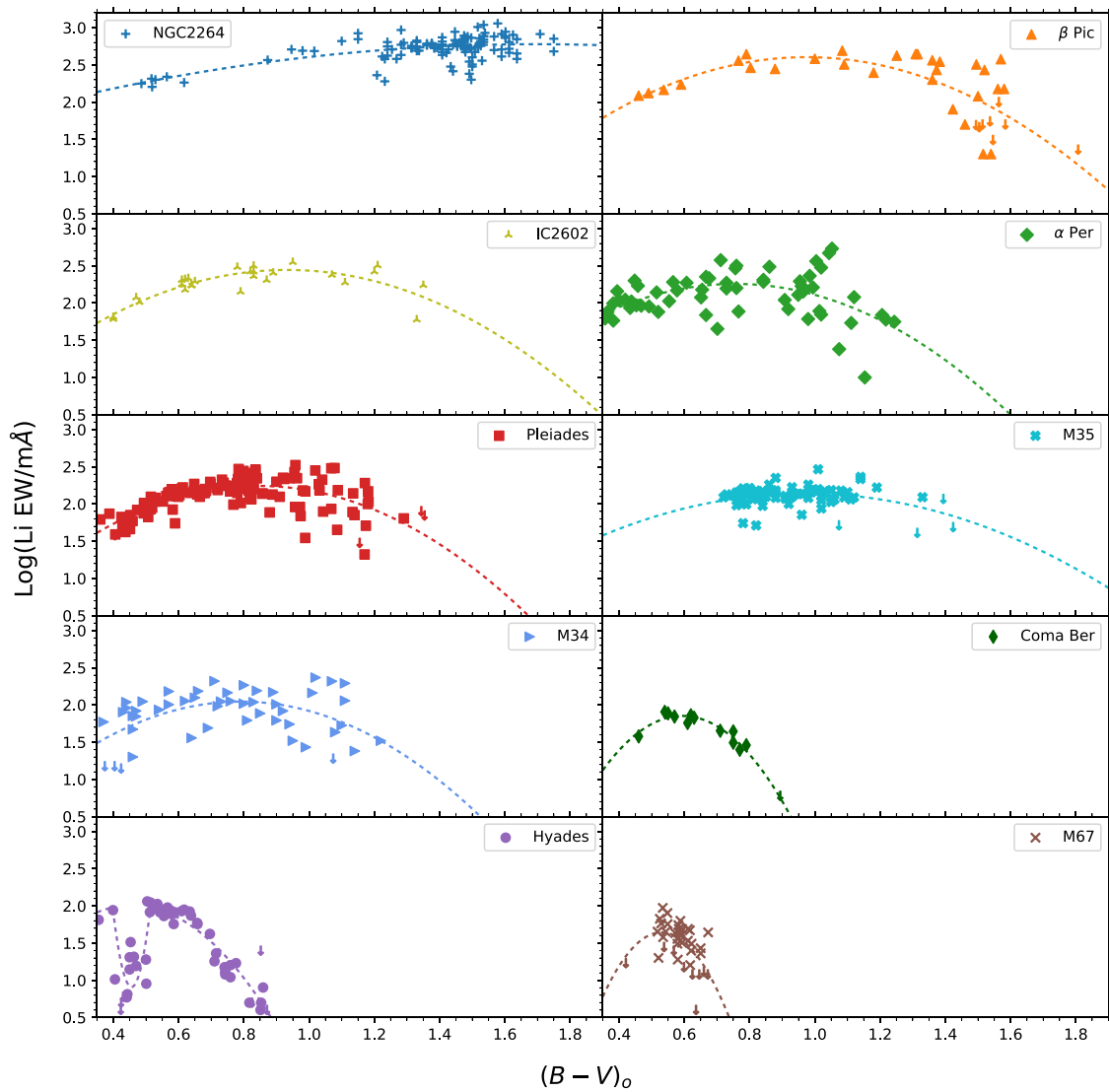
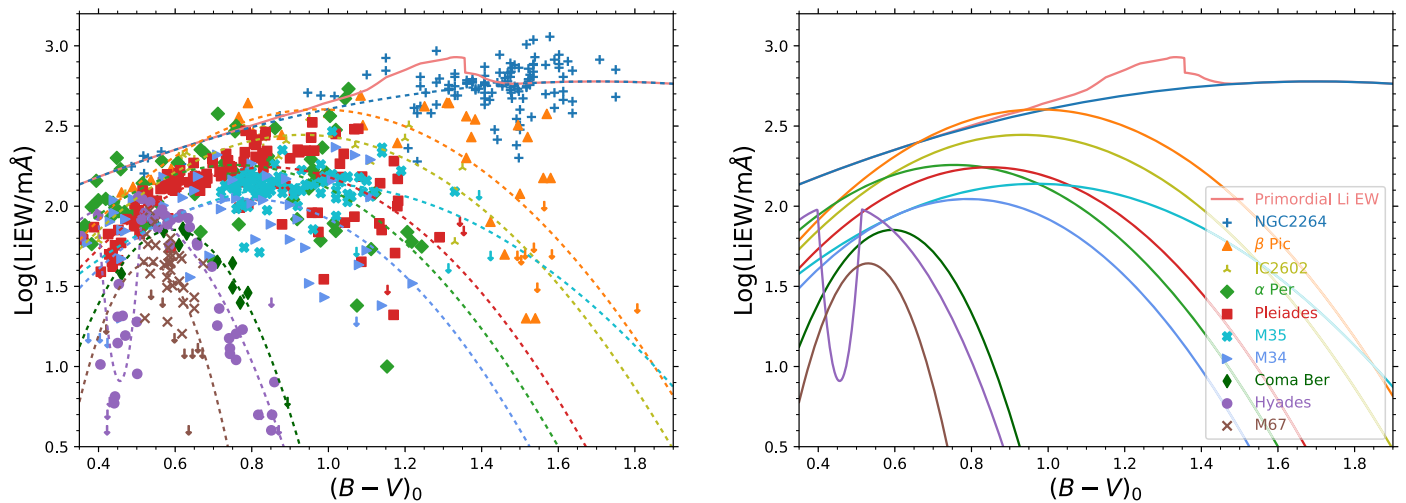


Figure 5. Lithium equivalent width measurements for our full data set, and final fits to each cluster. A second-order polynomial is a reasonable fit at all ages, outside of the lithium dip seen in the Hyades, which we model as a negative Gaussian.



(a) Full lithium dataset and fits to each cluster

(b) Fits only

Figure 6. Lithium equivalent width measurements for our full data set, and final fits to each cluster. As expected, lithium equivalent width decreases monotonically over time, but as a strong function of $B - V$ color. Primordial Li EW is estimated from MIST isochrones in conjunction with our fit to NGC 2264.

M34 (~ 200 Myr). By ~ 4 Gyr, stars have evolved off the main sequence, leaving no stars bluer than $B - V \approx 0.5$ in M67. Fits to each cluster are shown in Figures 5 and 6.

3.2.3. Li EW as a Function of Age

Unlike R'_{HK} , Li EW varies substantially across both age and $B - V$. As a result, the decline in lithium EW as a function of age must be fit across multiple slices of $B - V$. The polynomials fit to each cluster (Figure 5) define our preliminary fits $i'(t_m, b)$ as a function of $B - V$ at the age for each individual cluster (t_m). We examine 64 $B - V$ slices uniformly spaced between $B - V$ of 0.35 and 1.9. At each slice n , then, we have 10 values of $i'(t_m, b)$ corresponding to our 10 cluster data sets to which we add two additional points from primordial Li EW and Blue Lithium Depletion Boundary (BLDB, described below). From these, we determine the 64 fits, $i(t, b_n)$, as a function of age.

To help constrain the young end of the fits of Li EW and age, we approximate primordial Li EW using the MIST model isochrones (Choi et al. 2016) in conjunction with our NGC 2264 fit. In particular, we seek to extend the fit to this ~ 5 Myr cluster to the first age point in our grid, 1 Myr. At every $B - V$ value, we determine the corresponding effective temperature using the conversions from Pecaut & Mamajek (2013); we then find the Li abundance, $N(\text{Li})$, and initial stellar mass at 5 Myr from the MIST isochrones. Next, we find the Li abundance from the same initial mass star using the 1 Myr isochrones. We convert T_{eff} and the Li abundance to Li EW using the curve of growth in Soderblom et al. (1993) for $T_{\text{eff}} > 4000$ K, and that in Zapatero Osorio et al. (2002) for $T_{\text{eff}} \leq 4000$ K. The difference in Li EW between 1 and 5 Myr is added to the fit to NGC 2264 in order to determine the primordial Li EW at every $B - V$ value (Figure 6). The change found in Li EW between 1 and 5 Myr is only significant between $0.8 \lesssim B - V \lesssim 1.4$, and is negligible elsewhere.

We define the BLDB as the $B - V$ color for which stars redder than this boundary have no detectable lithium absorption, which we use to help constrain the older and redder range of fits to Li EW against age. Since the redder stars have deeper convective envelopes, they burn lithium faster than the bluer stars in the cluster. As a result, the nested polynomials of Figure 6 generally get narrower and move blueward over time, and thus the BLDB point moves blueward with increasing age. The BLDB is distinct from the classical LDB, which moves redder over time as a cluster's high-mass brown dwarfs deplete their lithium, while at the same time, all brown dwarfs evolve to redder colors as they cool over time, outside the brief deuterium-burning phase. We have defined the BLDB in order to add an additional data point to our fits for $B - V > 0.7$, as these are most important for constraining the ages of stars with $B - V > 1.4$, for which there are fewer literature measurements, especially at older ages. For each $B - V$ slice redward of 0.7, the fit to BLDB points gives an approximation of maximum age associated with $\log(\text{Li EW}) = 0.5$, or Li EW = 3.2 mÅ (Figure 7).

For each value of $B - V$, we use the mean value of $i, i'(t_m, b_n)$, from each cluster, in addition to the primordial lithium point and BLDB point, to fit the intermediate ages between the cluster ages and complete our grid. Unlike calcium, where the fits to individual clusters were independent of $B - V$, for lithium there is a strong $B - V$ dependence, and

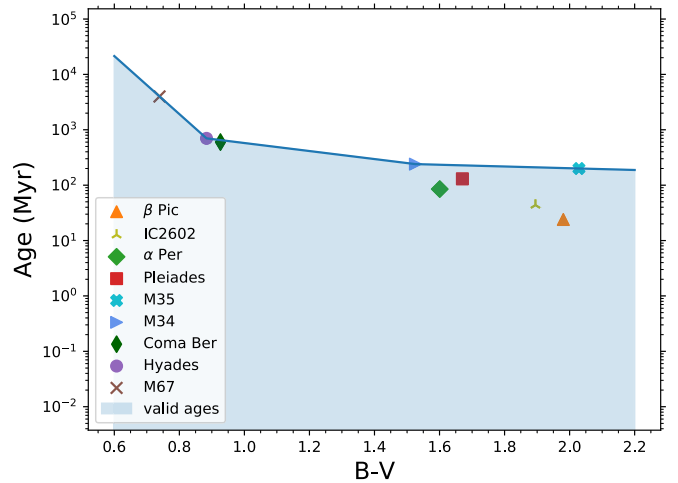


Figure 7. We introduce the concept of the Blue Lithium Depletion Boundary (BLDB)—which represents the age at each $B - V$ slice where lithium equivalent width drops below 3.2 mÅ—to constrain the lithium abundance at the oldest ages. Each point represents the $B - V$ magnitude where our polynomial fit to each cluster ($i'(t_m, b)$) goes below $\log(\text{Li EW}) = 0.5$ or 3.2 mÅ, which we adopt as the lowest detectable equivalent width of the lithium line. Redward of the BLDB point, we expect all stars in the cluster have no detectable lithium 6708 Å absorption. We adopt a piecewise-linear fit such that all clusters are at or below the fit.

for redder regions, the fit to the mean EW reaches unphysically small values. When cluster means drop below ~ 3 mÅ (0.5 on the log scale), we do not expect any detections, and clusters with $i'(t_m, b)$ below this value are not included in the fitting process.

As in Figure 8, we fit a 2–4 segment piecewise function to the cluster means, primordial Li EW, and BLDB point. The first segment is always between the Primordial Li EW value and NGC 2264, and the fit is constrained to decrease monotonically with age. Additionally, for $B - V$ slices inside the lithium dip ($0.41 \leq B - V \leq 0.51$), the final piecewise segment is constrained to go through the Hyades point. The locations of the segment breaks (except for the first break at NGC 2264) were free parameters. Weights for the cluster means were determined based on the relative proportion of stars the cluster had at a given $B - V$ slice in relation to the total number of stars. The BLDB point is given an uncertainty of about 0.15 dex, compared to 1 dex for clusters in poorly constrained regions. Although different functional forms were good fits to the decrease in lithium over time for some $B - V$ ranges, only the piecewise function was flexible enough to capture the shape more generally.

3.2.4. Astrophysical Scatter

With our grid of 64 $B - V$ slices and 1000 age slices for mean EW of lithium, $i(t, b)$, we next empirically determine the distribution of the residuals, $\mathcal{K}(|i(t, b), j(t)|)$, as we did with calcium (Figure 9). Residuals are with respect to the value of $i(t, b)$ evaluated at the age of each cluster and the $B - V$ value of the star, and upper limits are not considered in this step. As with calcium, we smooth the CDF of the residuals with Savitzky–Golay filters and take the derivative to convert to a PDF. We next fit exponential functions to the two tails, which we connect with the smoothed PDF, then normalize to have integral unity, defining $\mathcal{K}(|i(t, b), j(t)|)$. We also center the

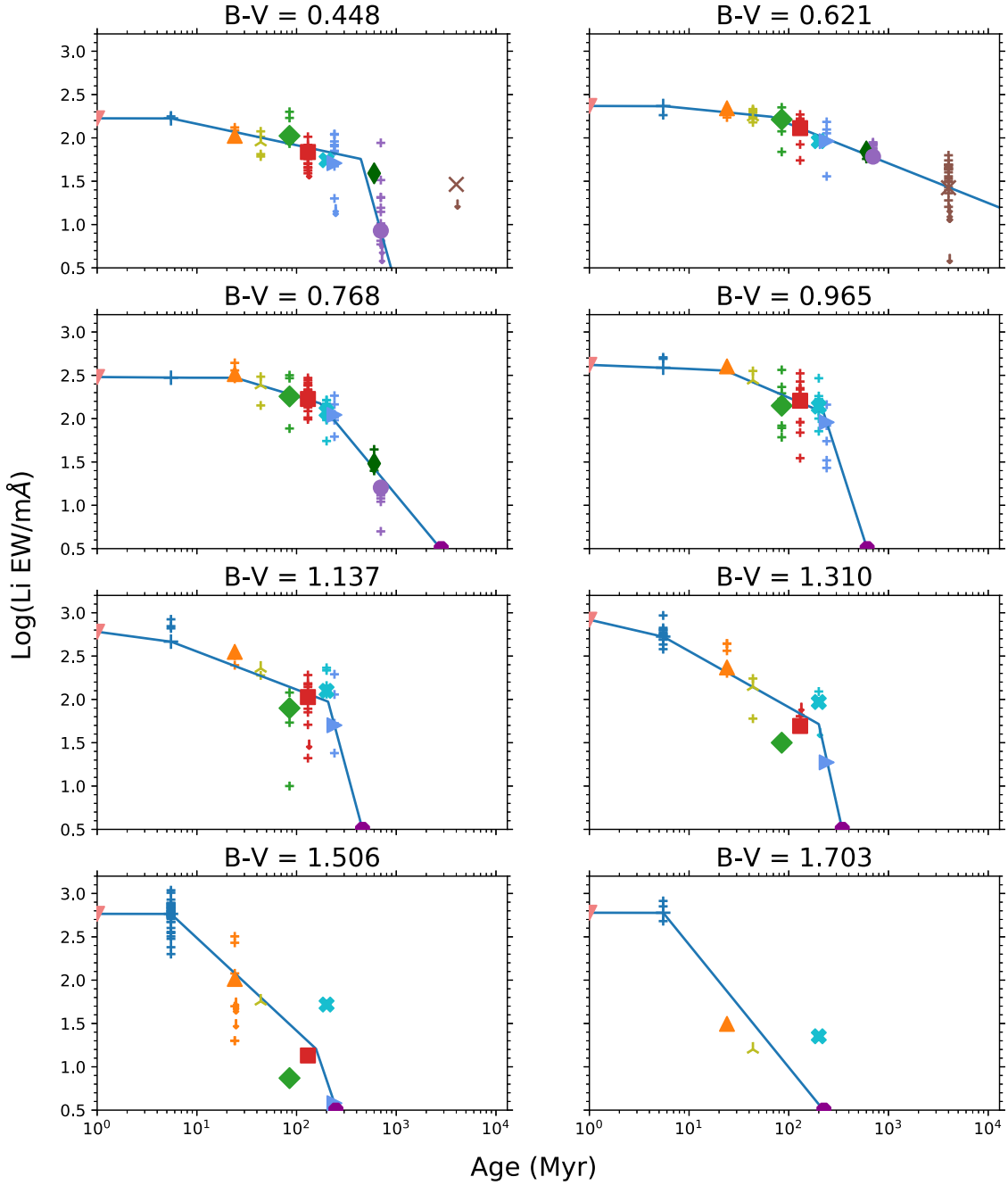


Figure 8. Examples of Li EW fits as a function of age $i(t, b_n)$, for eight out of 64 $B - V$ slices between 0.35 and 1.9 mag. Stars from each cluster within 0.05 mag of the $B - V$ slice are shown as small crosses if detections, or downward-facing arrows if upper limits. Cluster symbols are as in Figure 6, with an additional magenta BLDB point at $\log(\text{Li EW}) = 0.5$. Cluster means were fit with a flexible piecewise-linear function fixed to the primordial lithium point and NGC 2264. Cluster means were also weighted to give those with the most stars at each $B - V$ slice the most weight.

distribution at zero by subtracting off the residual median value of 0.033, which ensures that \mathcal{K} does not introduce a systematic bias toward older ages. Unlike calcium, we find no evidence for even a weak dependence on time of the standard deviation of the residuals ($j(t)$). As a result, the shape of \mathcal{K} is not a function of age or color, while the mean value is.

3.2.5. Lithium Posterior

Since we see no evidence for an age dependence in the astrophysical scatter, we take $j(t)$ to be a constant, and slightly

rewrite our posterior from Equation (16),

$$p(l, b, t|\hat{l}, \hat{b}) \propto \mathcal{N}(10^l|10^l, \sigma_l)\mathcal{N}(\hat{b}|b, \sigma_b)\mathcal{K}(l|i(t, b)). \quad (20)$$

To determine the age posterior for a single star, we construct a dense grid covering $B - V$ from 0.35 to 1.9 and age from 1 to 13,000 Myr. We use a grid of 64,000 elements ($64 B - V \times 1000$ age, logarithmically spaced in age), with the mean lithium abundance $i(t, b)$ calculated at each gridpoint. At each combination of (t, b) , we first marginalize over l by multiplying $\mathcal{K}(l|i(t, b))$ (our prior) by $\mathcal{N}(10^l|10^l, \sigma_l)$, a

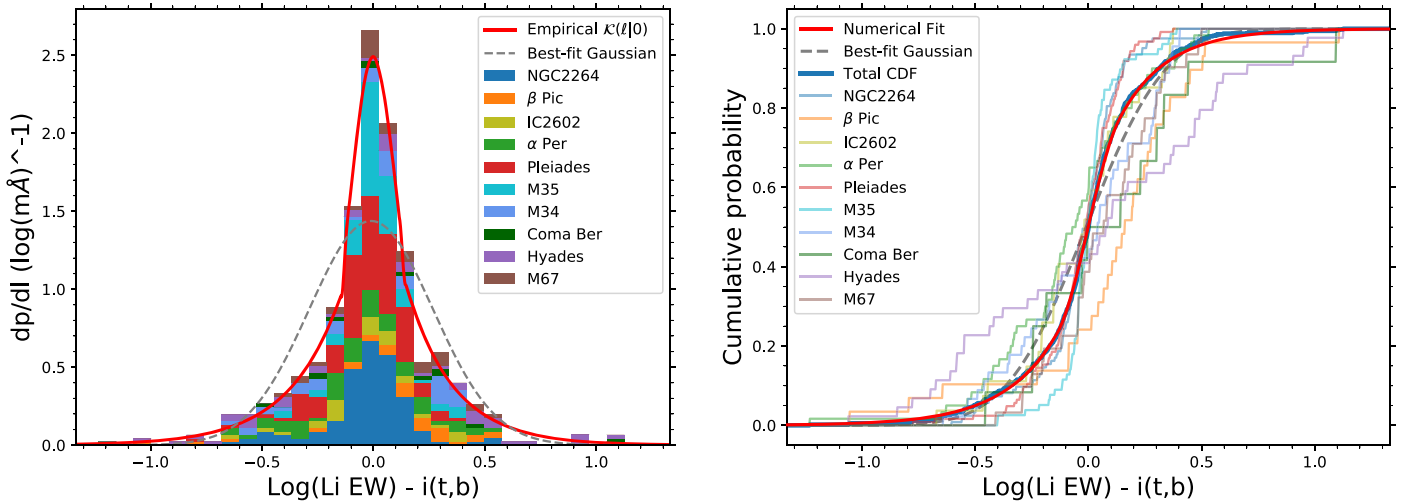


Figure 9. Left: numerically determined function $\mathcal{K}(l|i(t, b))$, which defines the astrophysical scatter in lithium abundance for stars of the same age and color, is plotted as a red line, along with the residuals of all cluster stars to the fit $i(t, b)$. Right: corresponding CDF. Similar to calcium, the numerical PDF has exponentially decreasing tails similar to a Gaussian distribution, but is significantly more peaked.

Gaussian representing the measurement of lithium EW and the associated measurement error, over an array of 1000 elements, logarithmically spaced in l between 0.5 and 1585 mÅ. To do this multiplication, however, we first convert $\mathcal{K}(l|i(t, b))$ to a function (similar to a log-normal) in linear space because the likelihood for \hat{l} , $\mathcal{N}(10^{\hat{l}}|10^l, \sigma_l)$, is defined in linear space. If no measurement uncertainty is given, we use a default error for σ_l of 15 mÅ, which is noted as a typical error by Soderblom et al. (1993). The products of these functions evaluated at all 1000 points are then summed, which gives the probability at that specific (t, b) gridpoint. We then marginalize over $B - V$ color by weighting each (t, b) gridpoint by the Gaussian likelihood for b , $\mathcal{N}(\hat{b}|b, \sigma_b)$, (assuming $\sigma_b = 0.01$ mag if no error is given) and summing over the product. To minimize computation time, instead of computing this probability at all (t, b) locations, we only evaluate gridpoints at 15 sampled values of b within $4 \cdot \sigma_b$ of \hat{b} , with all others set to 0. Having marginalized over both l and b , we are left with a marginalized posterior over only age, $p(t|\hat{l}, \hat{b})$.

If the measurement \hat{l} is an upper limit \hat{u} , we instead integrate $\mathcal{K}(l|i(t, b))$ from $-\infty$ to \hat{u} to find the probability at each (t, b) gridpoint. Thus, upper limits result in a plateau of probability at old ages, with a rapid drop-off toward younger ages.

4. Validation

4.1. Self-consistency of Age Posteriors

To test BAFFLES for self-consistency, we compare the posteriors for stars in moving groups and associations to the known ages of the groups, which we show for some clusters in Figures 10 and 11. We compute posteriors for each star in a cluster and then multiply the posteriors together, assuming the age determination for each star is independent, to produce a PDF for the age of the cluster as a whole. As an additional test, we repeat the process, but beforehand remove the target cluster from the input clusters used to fit $f(t)$ and $i(t, b)$ (though we leave the cluster in for computing $\mathcal{H}(r|f(t))$ and $\mathcal{K}(l|i(t, b))$). BAFFLES ages determined from calcium

posterior products match well with isochronal ages (Figure 10), though they have a slight shift toward older ages. We find that 6/9 clusters have ages older than their isochronal age, with only UCL+LCC, α Per, and Hyades being younger. Unsurprisingly, all three clusters lie above the fit in Figure 2. For the nine calcium clusters, Upper Sco, UCL+LCC, β Pic, Tuc/Hor, α Per, Pleiades, UMa, Hyades, and M67, we find the isochronal age to be within the 3.42%, 54.7%, 75.2%, 95.8%, 88.1%, 74.5%, 35.7%, 92.6%, and 66.9% confidence interval, respectively. We would expect two-thirds of the clusters to fall within the 68% confidence interval, and nearly all to fall within 95%, but here we have 4/9 within the 68% CI and 8/9 within the 95% CI. Notably, the largest outlier is Tuc/Hor (isochronal age within 95.8% CI), for which there are only six calcium stars. From Figure 2, Tuc/Hor appears to be the cluster farthest from the fit, and its distance below the fit pushes the predicted ages of its stars older. Going forward, larger sample sizes at these young ages are needed to better determine the time evolution of R_{HK}^l . For now, we caution that BAFFLES posteriors may slightly underestimate the errors from calcium, especially in age regimes that are less well-sampled.

A similar posterior product check with lithium clusters found good agreement with isochronal values (as seen in Figure 11).

We find 6/10 clusters have isochronal ages within the 68% confidence interval: β Pic, IC 2602, Pleiades, M35, M34, and Coma Ber. NGC 2264, α Per, Hyades, and M67 have isochronal ages within the 90.1%, 85.9%, 97.7%, and 85.2% confidence intervals, respectively, making 9/10 clusters within the 95% CI. We also find that half the clusters are younger than their isochronal ages (NGC 2264, IC 2602, Pleiades, M35, M34), while the other half are older, indicating no systematic offset in ages. The offset in the Hyades is likely due to three upper limits in the lithium dip with $\log(\text{Li EW})$ between ~ 0.6 and 0.8 dex, which significantly pull the posterior product to older ages. Computing the age of the Hyades while excluding these three upper limits (leaving 44 detections and three other upper limits), BAFFLES reports an age of 798 Myr and the isochronal age falls within our 74% confidence interval. Thus, it is likely more work needs to be done to properly model the

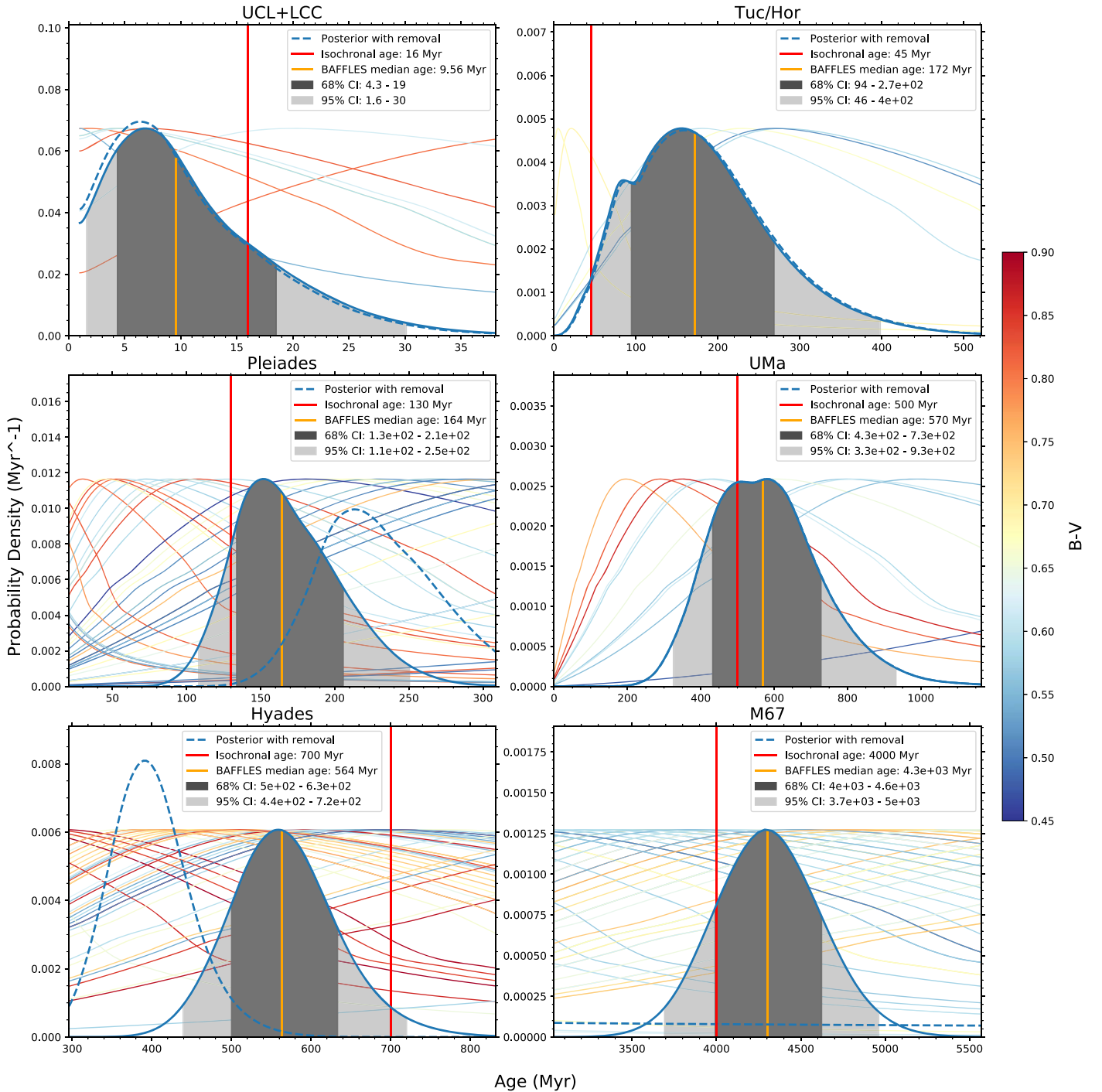


Figure 10. We test the validity of our calcium age posteriors by considering the product of PDFs from every star in one of our benchmark clusters, which should represent the PDF of the cluster age. We calculate the age posteriors for each star in the cluster (shown color-coded by $B - V$ and scaled to common height in the background), and finally multiply the age posteriors together to get the posterior product. Blue dashed line is the posterior product produced if we first omit the cluster from those used to calibrate BAFLES. “Isochronal Age” represents the more robustly determined ages from Table 1 that we use as the ages of our benchmark clusters. The mostly $1-2\sigma$ agreement suggests that the median age and uncertainties we find with BAFLES are reasonable, though uncertainties reported by BAFLES may be slightly underestimated.

lithium dip to produce robust posteriors for stars within the dip. As with calcium, a product of posteriors is very sensitive to each individual posterior, such that a single nonmember—or errors in color or lithium abundance—can move the product significantly from the age of the group as a whole. We conclude that the age posteriors generated by BAFLES from lithium abundances are consistent with the ages of our benchmark clusters.

4.2. Moving Groups

We further examine the accuracy of BAFLES age posteriors by considering the ages derived for multiple stars in moving groups not included in our set of benchmark clusters. As before, we compute age PDFs for each star in the moving group and then multiply the PDFs together to find an age for the group as a whole, which we compare (in Figure 12) to isochronal ages from Bell et al. (2015).

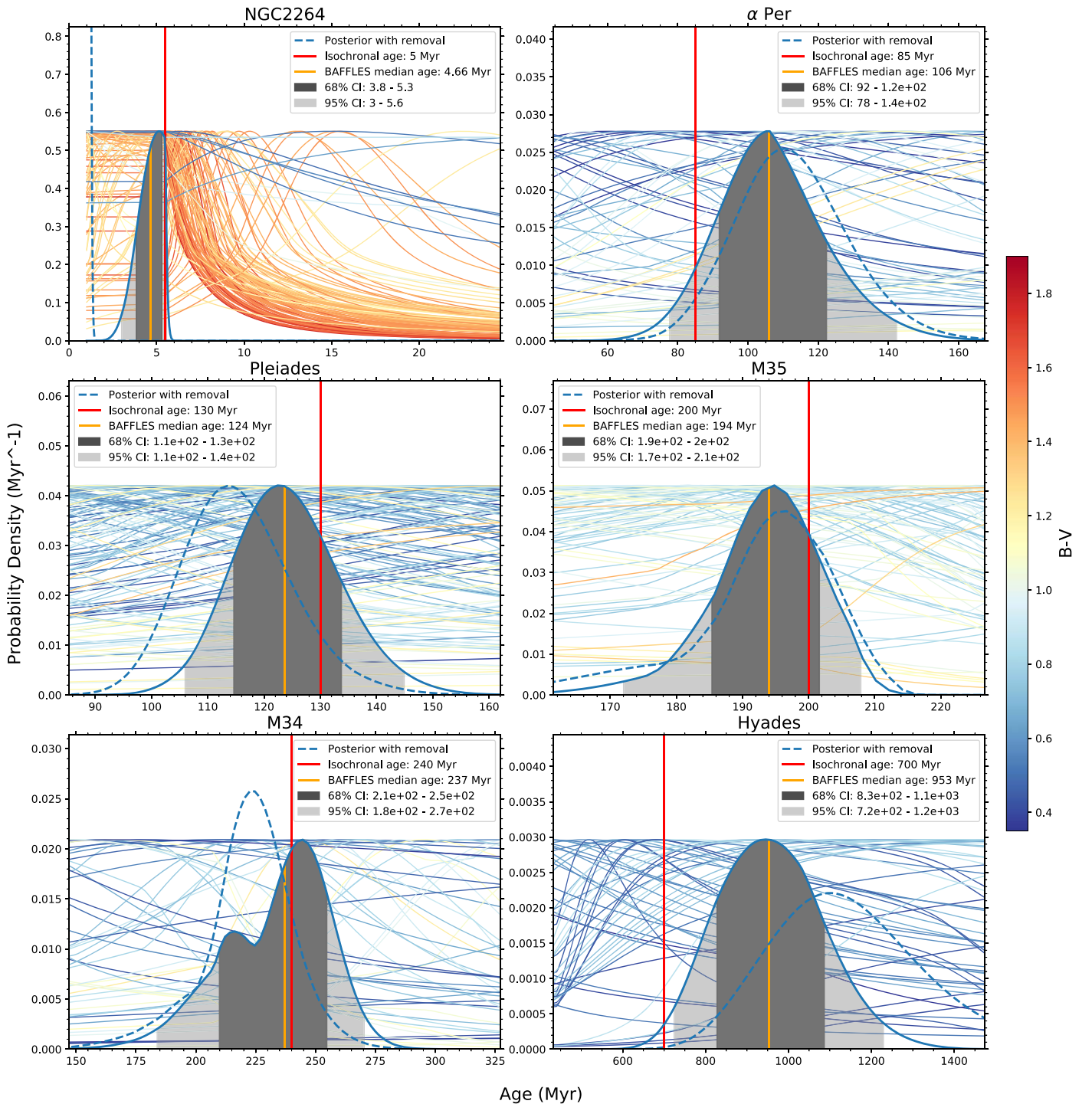


Figure 11. Following Figure 10, we test the validity of our lithium posteriors. Our ages are consistent with isochronal ages to within 68% confidence intervals for 6 of our 10 clusters, and to within 95% confidence intervals for 9/10 clusters.

Lithium EWs for AB Dor and Tuc/Hor are from Mentuch et al. (2008), and $B - V$ magnitudes used are provided in Table A1 in the Appendix. From AB Dor, we removed the following binaries: HD 13482A, HD 13482B, HD 17332B, HD 217379N, and HD 217379S. We also removed a star with large $B - V$ uncertainties (error $\gtrsim 0.15$ mag): BD+21 418B. From Tuc/Hor, we removed the binaries: AF Hor, BS Ind, HIP 116748N, HIP 116749S, TYC 7065-0879N, and TYC 7065-0879S. We additionally removed the following stars with error $\gtrsim 0.15$ mag: EXO 0235.2-5216, CD-58

553, Smethells 86, CT Tuc, Smethells 165, and Smethells 173.

We derive ages for AB Dor 127^{+35}_{-28} Myr, and for Tuc/Hor 35^{+11}_{-10} Myr, as in Figure 12. These ages are within 1σ of isochronal ages (AB Dor 149^{+51}_{-19} Myr, Tuc/Hor 45^{+4}_{-4} Myr) from Bell et al. (2015). We caution against using the ages we derive for these moving groups, however, since our posterior products can be significantly biased by a single star with incorrect values (either lithium abundance, B or V) or with an incorrect membership determination.

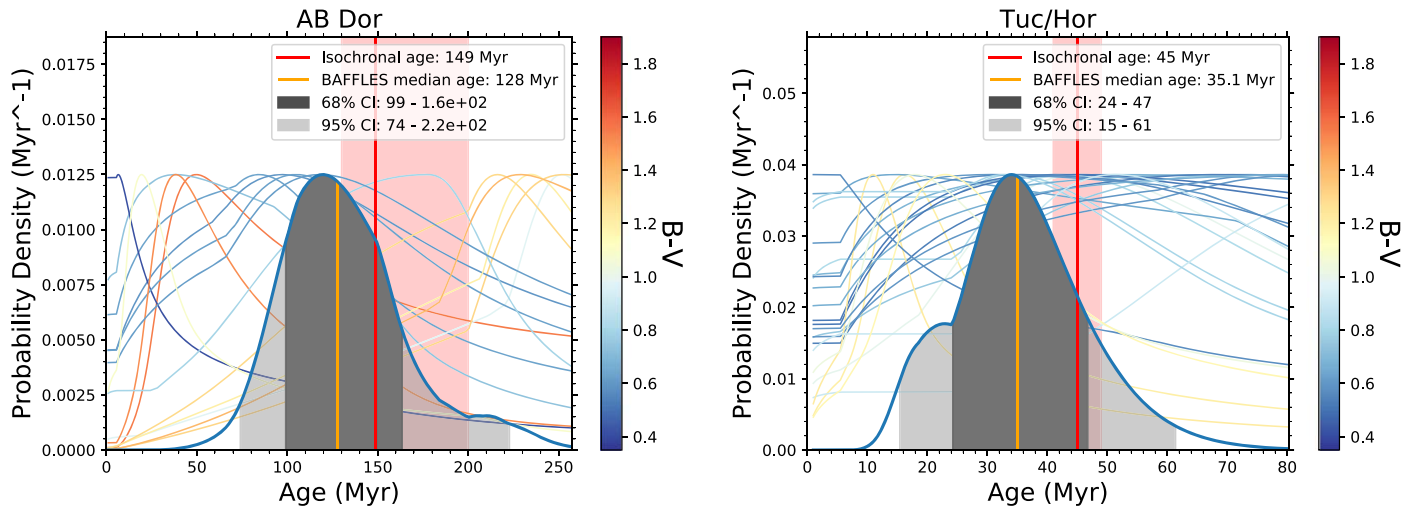


Figure 12. We compute age posteriors for AB Dor and Tuc/Hor from the product of the posteriors of stars in each moving group. Our computed ages agree with isochronal values to within 1σ , suggesting that our lithium-derived posteriors are generally accurate. Data for AB Dor and Tuc/Hor is from Mentuch et al. (2008) and isochronal ages are from Bell et al. (2015).

5. Analysis

5.1. Notable Stars: TW PsA, HR 2562, and HD 206893

We show examples of ages derived using BAFLES for three field stars associated with substellar companions: the brown dwarf hosts HR 2562 and HD 206893, and the stellar companion to the exoplanet host Fomalhaut, TW PsA. Age sets the formation timescale for these substellar companions, and in the case of the brown dwarfs, the model mass derived for these objects depends directly on the assumed age.

TW PsA is a stellar companion to the A3V star Fomalhaut with a bright debris disk and planetary companion. The system’s age has been estimated by Mamajek (2012) to be 440 ± 40 Myr by combining independent age estimates from isochrones, rotation rate, X-ray luminosity, and lithium abundance. From lithium alone, Mamajek (2012) estimates an age of 360 ± 140 Myr by comparing the Li EW of TW PsA, with values $B - V = 1.1$ (V is taken from Keenan & McNeil (1989) and B from Cutri et al. (2003)) and $\text{Li EW} = 33 \pm 2$ (Barrado y Navascués et al. 1997), to the Li EW in the clusters Pleiades, M34, UMa, and Hyades. Using these same values of $B - V$ and Li EW as input to BAFLES, we report an age of 295 Myr with a 68% confidence interval between 213 and 371 Myr (third panel of Figure 13), consistent with the Mamajek (2012) lithium age, but a factor of ~ 1.5 too young for the final adopted age. However, at $B - V = 1.1$, we are limited by our cluster samples, which have lithium detections up to the age of M34 (240 Myr) and nondetections at the age of Coma Ber (600 Myr), but no information in between. Thus, interpolations to older ages at this $B - V$ are difficult with our current data set.

We also combine our age PDF with that for the A star Fomalhaut from Nielsen et al. (2019), 750_{-190}^{+170} Myr, with our PDF (middle-right plot of Figure 13), to get a final age for the system, 356_{-75}^{+58} Myr. Because the distribution from BAFLES is significantly narrower than that from Nielsen et al. (2019), the product age changes little, yet this serves as an example of how an age posterior allows ages from BAFLES to be robustly combined with ages from other sources.

HR 2562 is an F5V star around which a brown dwarf companion was discovered with the Gemini Planet Imager in

2016 (Konopacky et al. 2016). Asiain et al. (1999) estimated the age to be 300 ± 120 Myr based on space motions and evolutionary model-derived ages. Casagrande et al. (2011), using Strömgren photometry and isochrones, derive a Bayesian age of 0.9–1.6 Gyr (68% confidence interval). From calcium alone, with $\log(R'_{HK}) = -4.551$ (Gray et al. 2006), we report an age of 1400 Myr (68%CI: 690–3700 Myr). From lithium alone, using $\text{Li EW} = 21 \pm 5$ (Mesa et al. 2018) and $B - V = 0.45 \pm .02$ (Høg et al. 2000), we find an age of 0.7 Gyr (68%CI: 0.5–1.8 Gyr). HR 2562 is in the very center of the lithium dip, and so the depletion at this color is poorly constrained, given that the Hyades is the only data set in which the dip is visible and there are no older clusters in our sample at this color. Combining these posteriors, our final age is 660 Myr, with a 68% confidence interval between 520 and 1100 Myr, consistent with the age range 300–900 Myr adopted by Konopacky et al. (2016).

HD 206893 is an F5V star with a brown dwarf companion inside its debris disk (Milli et al. 2017). Pace (2013) derives its age to be 860 ± 710 Myr from chromospheric activity. On the other hand, David & Hillenbrand (2015) derive an age of 2.1 Gyr with 68% CI between 1.2 and 4.7 Gyr using a Strömgren photometry fit to stellar atmosphere models, though given the long main-sequence lifetime of early F stars, this method is not particularly sensitive to the differences between young and intermediate ages (e.g., Nielsen et al. 2013). Milli et al. (2017) adopts an age range between 200 and 2100 Myr. Using a value of $\log(R'_{HK}) = -4.466$ (Gray et al. 2006), from calcium emission alone, we derive a median age of 910 Myr (68%CI: 410–2700 Myr). From lithium absorption with $\text{Li EW} = 28.5 \pm 7 \text{ mÅ}$ (Delorme et al. 2017) and $B - V = 0.44 \pm 0.02$ (Høg et al. 2000), we report an age of 1.3 Gyr (68%CI: 0.5–5.5 Gyr), though like HR 2562, HD 206893 is also in the center of the lithium dip. Our final age after combining these two posteriors is 570 Myr, with a 68% confidence interval between 380 and 1000 Myr, consistent with literature ages.

We find that BAFLES age posteriors for these field stars are consistent with literature ages. Both HR 2562 and HD 206893 are within the lithium dip, and more data are needed to accurately map the depletion of lithium at these ages and

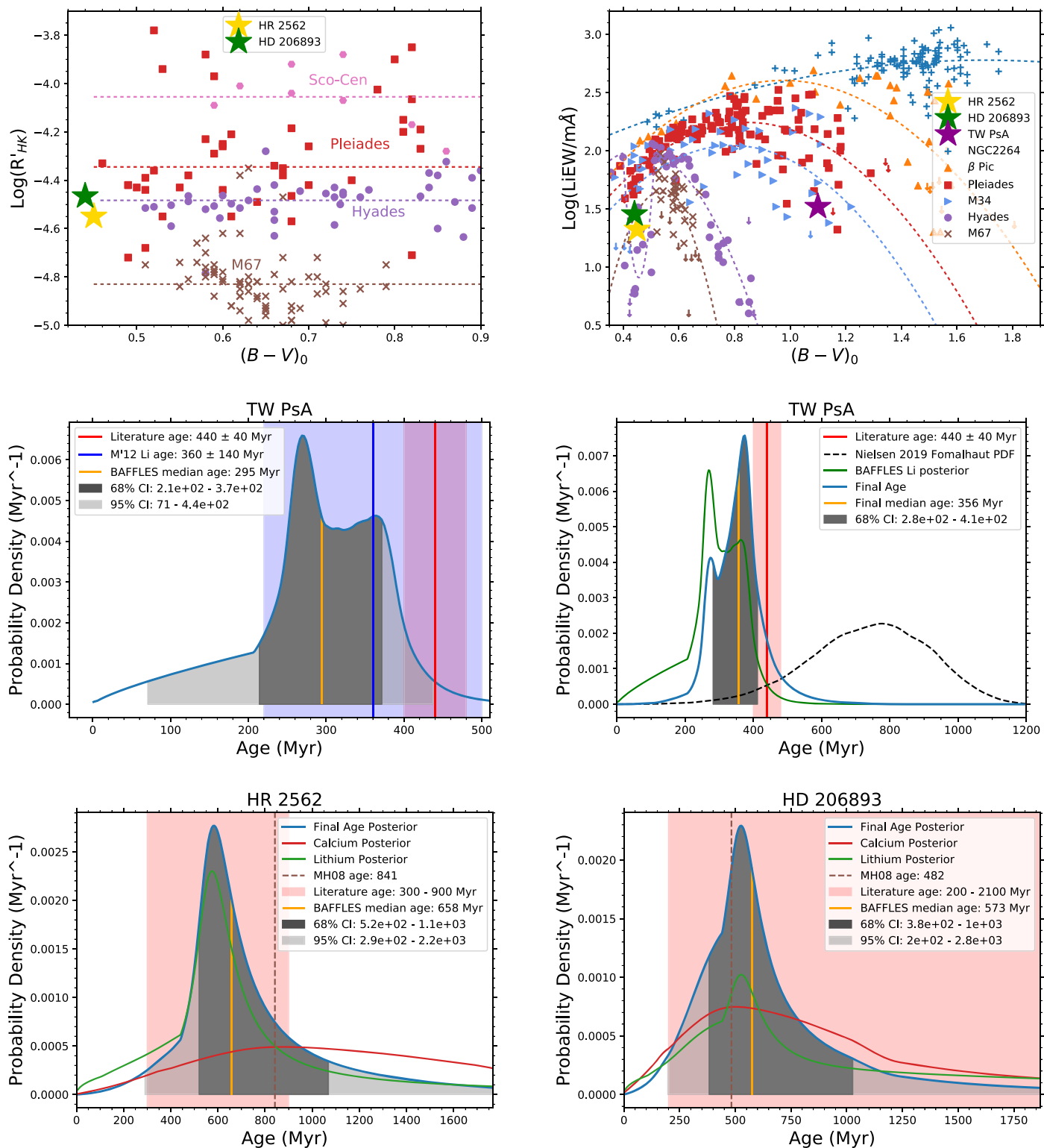


Figure 13. BAFPLES age posteriors for three notable field stars from calcium R'_{HK} and lithium equivalent width. The top panel shows the measurements of $B - V$, R'_{HK} , and Li EW of the stars in comparison with a subset of our benchmark clusters. We then compare the age posterior computed using BAFPLES to ages from the R'_{HK} polynomial in Mamajek & Hillenbrand (2008) (“MH08 age,” though we again note that Mamajek & Hillenbrand (2008) advocate a modified R'_{HK} relation incorporating additional correlations as well) and literature ages from Mamajek (2012), Konopacky et al. (2016), and Milli et al. (2017) for TW PsA, HR 2562, and HD 206893, respectively. For HR 2562 and HD 206893, age posteriors for calcium and lithium are multiplied together to find a final age. Middle-right plot demonstrates combining a posterior from BAFPLES with the PDF from a different source, in this case the age PDF for Fomalhaut derived by Nielsen et al. (2019).

colors. In general, however, lithium-based ages are often more constraining than calcium-based ones, given that the astrophysical scatter in R'_{HK} is a more significant fraction of the total

range of R'_{HK} . Nevertheless, the combination of these two methods tends to increase the precision on the final age posterior.

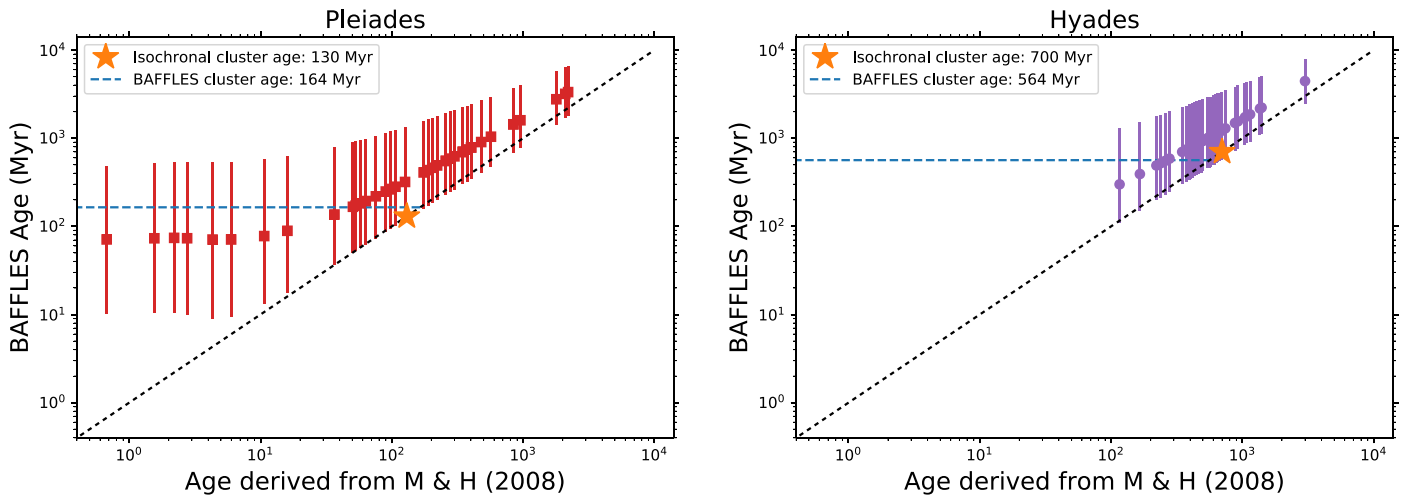


Figure 14. Comparison of BAFPLES calcium age posteriors to stellar ages derived from the polynomial fit (Equation (3)) from Mamajek & Hillenbrand (2008). Error bars indicate the 68% confidence interval from BAFPLES. As expected from the shape of the polynomial fit to R'_{HK} vs. time (Figure 2), the polynomial method tends to be biased toward younger ages. BAFPLES produces systematically older ages for individual stars, yet the product of these individual posteriors (Figure 10) shows that taken together, these posteriors are close to the correct age for the cluster as a whole.

5.2. Comparison to Previous Methods

The BAFPLES median ages are systematically older than those derived from the Mamajek & Hillenbrand (2008) R'_{HK} polynomial, despite relying on the same clusters and very similar fits to the clusters (Figure 2). In the Pleiades and Hyades, for example, the median age we derive for each star with BAFPLES (Figure 14) is older than the age given by the polynomial fit of Mamajek & Hillenbrand (2008). As described in Section 1.2, this is largely a result of the shape of the polynomial fit to mean R'_{HK} as a function of time, which becomes flatter at younger ages and thus favors younger ages. Our uniform star formation rate prior mitigates this effect, pushing each age posterior back toward older values.

5.3. BAFPLES Ages for Young, Nearby Stars

We use our method, BAFPLES, for a sample of 2630 nearby stars that appear in recent compilations of lithium measurements, R'_{HK} measurements, or direct imaging surveys. In Table 2, we derive the ages of stars from the analysis of two direct imaging planet surveys by Nielsen & Close (2010), from the SEEDS High-contrast Imaging Survey of Exoplanets and Disks (Brandt et al. 2014b), from the compilation of R'_{HK} values by Boro Saikia et al. (2018), and from the lithium measurements in the spectroscopic survey of Guillout et al. (2009). Boro Saikia et al. (2018) compiled R'_{HK} values from a number of previous literature surveys, including Arriagada (2011), Wright et al. (2004), Isaacson & Fischer (2010), Henry et al. (1996), Gray et al. (2006), Hall et al. (2009), Lovis et al. (2011), Bonfils et al. (2013), Duncan et al. (1991), and Baliunas & Vaughan (1985). Guillout et al. (2009) acquired lithium and $H\alpha$ measurements of several hundred field stars.

We compute age posteriors for each unique star from R'_{HK} and Li EW separately, and when both are available, we multiply these posteriors to determine a final age. For stars with multiple entries, we first compute the mean values of $B - V$, R'_{HK} and Li EW over all measurements, then use these means to find the age posteriors.

6. Conclusion

We have implemented a Bayesian framework, BAFPLES, for determining the posterior PDF on stellar age from measurements of R'_{HK} calcium emission and/or $B - V$ color and Li EW lithium abundance. Importantly, BAFPLES properly incorporates astrophysical scatter and physical priors. In developing this framework:

1. We empirically determine the evolution over time of spectral indicators R'_{HK} and Li EW for clusters of stars with well-characterized isochronal ages.
2. Using these benchmark clusters, we derive a numerical prior to derive age as a function of R'_{HK} for stars with $0.45 \leq B - V \leq 0.9$ and age as a function of $B - V$ and Li EW for $0.35 \leq B - V \leq 1.9$.
3. From our tests, the method appears self-consistent and produces robust posteriors on age, though the uncertainty on ages derived from calcium may be slightly underestimated.

Looking ahead to future space missions, accurate ages become increasingly important. In the next few years, Gaia is expected to discover thousands of exoplanets and brown dwarfs from measuring precise astrometry of host stars (Perryman et al. 2014). The James Webb Space Telescope, planned to launch in 2021, should be able to survey the nearest and youngest of these Gaia targets to directly image the orbiting planets in the thermal infrared, where intermediate-age (~ 100 Myr–1 Gyr) planets have more favorable contrasts than in the near-infrared (Beichman et al. 2019). Likewise, the European Extremely Large Telescope (e.g., Tamai et al. 2016), Thirty Meter Telescope (e.g., Simard et al. 2016), and Giant Magellan Telescope (e.g., Fanson et al. 2018) will in the near future advance our ability to directly image exoplanets. For the next generation of telescopes, we will need stellar ages to help choose the targets for observing, because younger planets are more luminous and thus easier to detect and characterize via direct imaging. Similarly, when exoplanets are discovered, the ages of the host stars will allow mass determination for the self-luminous stellar companions. Additionally, significant evolution of planetary systems is predicted over hundreds of Myr

Table 2
(Continued)

Name	R.A. h m s	Decl. h m s	Sp. Type	$B - V$ mag	$\log R'_{HK}$	Li EW (mÅ)	Reference	R'_{HK} Age					Li EW Age					Final Age				
								at Posterior CDF Value (Myr)					at Posterior CDF Value (Myr)					at Posterior CDF Value (Myr)				
								2.5%	16%	50%	84%	97.5%	2.5%	16%	50%	84%	97.5%	2.5%	16%	50%	84%	97.5%
HD 142	00 06 19.18	-49 04 30.68	F7V	0.52	-4.77		(3)	1040	2300	4170	7500	11700						1040	2300	4170	7500	11700
HD 166	00 06 36.78	+29 01 17.41	G8	0.75	-4.36		(3)	63	193	478	1740	6830						63	193	478	1740	6830
HD 232102	00 06 37.38	+55 27 21.72	K0	0.92		4	(4)						342	493	754	1050	1420	342	493	754	1050	1420
HD 283	00 07 32.54	-23 49 7.40	G9.5V	0.80	-4.98		(3)	2710	5480	8700	11500	12800						2710	5480	8700	11500	12800
HD 299	00 07 52.09	+55 34 37.35	G0	0.60		67	(4)						293	983	3540	8990	12400	293	983	3540	8990	12400
HD 361	00 08 16.36	-14 49 28.17	G1V	0.62	-4.80		(3)	1220	2650	4730	8080	11900						1220	2650	4730	8080	11900
HD 377	00 08 25.75	+06 37 0.49	G2V	0.63	-4.35	150	(2), (3)	61	188	467	1720	6780	28	117	752	5360	11500	42	103	209	477	1480
HD 375	00 08 28.47	+34 56 4.35	F8	0.61	-4.86		(3)	1660	3520	6050	9290	12300						1660	3520	6050	9290	12300
HD 330	00 08 4.69	+53 47 46.50	F8V	0.59		71	(4)						264	921	3490	9000	12400	264	921	3490	9000	12400
HD 400	00 08 40.94	+36 37 37.65	F8IV	0.50	-4.80		(3)	1200	2620	4680	8020	11900						1200	2620	4680	8020	11900
HD 457	00 08 59.68	-39 44 13.78	G0V	0.62	-4.95		(3)	2440	5000	8110	11200	12700						2440	5000	8110	11200	12700
HD 483	00 09 19.44	+17 32 2.12	G2III	0.64	-4.58		(3)	338	827	1690	4150	9850						338	827	1690	4150	9850
HD 449	00 09 2.85	+09 50 59.88	G5	0.71	-4.93		(3)	2250	4640	7640	10800	12600						2250	4640	7640	10800	12600
HD 531B	00 09 51.30	+08 27 11.89	G7V	0.72	-4.35		(3)	62	191	474	1730	6810						62	191	474	1730	6810
HD 531A	00 09 51.65	+08 27 11.40	G6V	0.72	-4.32		(3)	45	146	380	1500	6340						45	146	380	1500	6340
HD 531	00 09 51.65	+08 27 11.41	G6V +G7V	0.72	-4.33		(3)	50	158	405	1560	6480						50	158	405	1560	6480
HD 564			G2/3V	0.59	-4.72		(3)	809	1820	3400	6610	11400						809	1820	3400	6610	11400

Table 2
(Continued)

Name	R.A.	Decl.	Sp. Type	$B - V$	$\log R'_{HK}$	Li EW	Reference	R'_{HK} Age					Li EW Age					Final Age				
								at Posterior CDF Value (Myr)					at Posterior CDF Value (Myr)					at Posterior CDF Value (Myr)				
								2.5%	16%	50%	84%	97.5%	2.5%	16%	50%	84%	97.5%	2.5%	16%	50%	84%	97.5%
h m s	h m s	mag	(mÅ)																			
	00	-50																				
	09	16																				
	52.82	4.17																				
* 6 Cet	00	-15	F8VFe-	0.49	-4.79		(3)	1170	2560	4590	7930	11900										
	11	28	0.8CH-																			
	15.85	4.74	0.5																			
V344 And	00	+30	K0V	0.76	-4.30		(3)	38	127	339	1390	6110										
	11	26																				
	22.44	58.47																				
HD 750	00	-57	K1V	0.89	-4.68		(3)	610	1410	2710	5710	10900										
	11	28																				
	35.79	21.18																				
* tet Scl	00	-35	F5V	0.46	-4.64		(3)	496	1170	2290	5110	10600										
	11	07																				
	44.02	59.23																				
BD+64 9	00	+65	F8	0.57		3	(4)						1230	4110	8380	11600	12800	1230	4110	8380	11600	12800
	12	36																				
	0.92	17.53																				
HD 804	00	+20	G5	0.67	-4.97		(3)	2600	5290	8460	11400	12700										
	12	14																				
	28.33	3.65																				
HD 870	00	-57	K0V	0.78	-4.75		(3)	951	2110	3870	7170	11600										
	12	54																				
	50.25	45.40																				
HD 984	00	-07	F7V	0.52	-4.34		(3)	57	177	444	1660	6670										
	14	11																				
	10.25	56.81																				
HD 1108	00	-68	G6V	0.69	-4.80		(3)	1190	2590	4640	7980	11900										
	15	31																				
	4.63	48.36																				

Note. R.A. and decl. from Simbad online services. Bold values indicate the median age for each distribution.

References. (1) Nielsen & Close 2010; (2) Brandt et al. 2014b; (3) Boro Saikia et al. 2018; (4) Guillout et al. 2009.

(This table is available in its entirety in machine-readable form.)

(Chiang & Murray 2002; Ford & Rasio 2008; Freikh et al. 2019), and having a large number of giant planet systems with well-characterized ages will allow these predictions to be directly tested. *BAFFLES* will fill a unique role in producing robust age posteriors in a uniform way for lower-mass field stars.

We thank Eric Mamajek for helpful conversations that improved this manuscript, and for compiling “The Lithium Plot,”⁷ which inspired some of this work. This research has made use of the SIMBAD and VizieR databases, operated at CDS, Strasbourg, France. R.D. acknowledges support from the Fonds de Recherche du Québec. Supported by NSF grants AST-1411868 (E.L.N., B.M.), and AST-1518332 (R.J.D.R.). Supported by NASA grants NNX14AJ80G (E.L.N., B.M.), NNX15AC89G and NNX15AD95G (B.M., R.J.D.R.), 80NSSC17K0535 (B.M., E.L.N., R.J.D.R.), and NASA Hubble Fellowship grant HST-HF2-51405.001-A (I.C.).

Software: Astropy (Astropy Collaboration et al. 2013), SciPy (Virtanen et al. 2020).

Appendix B – V References

Table A1 gives $B-V$ values for stars compiled from the literature.

Table A1
 $B-V$ References for AB Dor, Tuc/Hor, and β Pic

Name	SpT	Moving Group	$B - V$	Reference
GSC 08894-00426	M5Ve	AB Dor	1.551	(10), (9)
HD 217343	G5V	AB Dor	0.64	(2)
HD 218860	G8V	AB Dor	0.738	(2), (9)
HD 224228	K2V	AB Dor	0.985	(7)
HD 35650	K6V	AB Dor	1.311	(7), (9)
HD 45270	G1V	AB Dor	0.602	(7)
HD 65569	F5III	AB Dor	0.42	(2)
HIP 14809	G5	AB Dor	0.63	(2)
HIP 17695	M3.0V	AB Dor	1.511	(7), (9)
HIP 26369	K6Ve	AB Dor	1.205	(7)
HIP 31878	K7V(e)	AB Dor	1.297	(7), (9)
HIP 6276	G9V	AB Dor	0.8	(2)
HR 2468	G1/2V	AB Dor	0.62	(6)
UY Pic	K0V	AB Dor	1.094	(2), (9)
V372 Pup	M1Ve	AB Dor	1.402	(7), (9)
CD-53 544	K6Ve	Tuc/Hor	1.209	(2), (10)
CD-60 416	K5Ve	Tuc/Hor	1.0	(2)
CPD-64 120	K1Ve	Tuc/Hor	0.807	(2), (9)
HD 13183	G7V	Tuc/Hor	0.69	(2)
HD 13246	F7V	Tuc/Hor	0.52	(2)
HD 8558	G7V	Tuc/Hor	0.667	(2), (9)
HD 9054	K1V	Tuc/Hor	0.91	(4)
HIP 105388	G7V	Tuc/Hor	0.65	(9)
HIP 108422	G9IV	Tuc/Hor	0.83	(2)
HIP 1113	G8V	Tuc/Hor	0.756	(2), (9)
HIP 1481	F8V	Tuc/Hor	0.54	(2)
HIP 16853	G2V	Tuc/Hor	0.6	(2)
HIP 21632	G3V	Tuc/Hor	0.61	(2)
HIP 22295	F7V	Tuc/Hor	0.515	(2), (9)

Table A1
(Continued)

Name	SpT	Moving Group	$B - V$	Reference
HIP 2729	K4Ve	Tuc/Hor	1.226	(9)
HIP 30030	G0V	Tuc/Hor	0.57	(2)
HIP 30034	K1V(e)	Tuc/Hor	0.805	(2), (9)
HIP 32235	G6V	Tuc/Hor	0.575	(2), (9)
HIP 33737	K2V	Tuc/Hor	1.036	(2), (9)
HIP 490	G0V	Tuc/Hor	0.6	(1)
HIP 9141	G4V	Tuc/Hor	0.673	(2), (9)
TYC 7600-0516-1	K1V(e)	Tuc/Hor	0.898	(2), (9)
TYC 5882-1169-1	K3/4	Tuc/Hor	1.166	(2), (9)
G 271-110	M4	β Pic	1.803	(10)
	+ > L0			
BD+30 397B	M2	β Pic	1.5	(1)
BD+05 378	K6	β Pic	1.309	(4), (9)
PM J03325+2843	M4+M4.5	β Pic	1.542	(10)
UCAC2 36944937	M5	β Pic	1.0	(10)
V1005 Ori	M0	β Pic	1.373	(2), (9)
CD-57 1054	M0.5	β Pic	1.383	(2), (9)
UCAC3 176-23654	M2.9	β Pic	1.49	(10)
AO Men	K6.5	β Pic	1.251	(2), (9)
HD 139084	K0	β Pic	0.803	4, (9)
ASAS J164301-1754.4	M0.6	β Pic	1.36	(3), (8)
CD-27 11535	K5	β Pic	1.084	(2), (9)
HD 155555C	M4.5	β Pic	1.54	(4)
GSC 08350-01924	M3	β Pic	1.46	(4)
CD-54 7336	K1	β Pic	0.766	(2), (9)
HD 161460	K0	β Pic	1.495	(4), (9)
HD 319139	K6	β Pic	0.79	(2)
GSC 07396-00759	M1.5	β Pic	1.36	(4)
PZ Tel	K0	β Pic	0.878	(2), (9)
1SWASP J191028.18-231948.0	M4.0	β Pic	1.533	(5)
CD-26 13904	K4	β Pic	1.09	(2)
UCAC3 116-474938	M4	β Pic	1.56	(10)
SCR J2010-2801	M2.5	β Pic	1.5	(10)
	+M3.5			
AU Mic	M1	β Pic	1.423	(9)
CPD-72 2713	K7+K5	β Pic	1.315	(2), (9)
WW PsA	M4	β Pic	1.516	(7), (9)
TX PsA	M4.5	β Pic	1.57	(4)
UCAC4 494-001142	M3.9	β Pic	1.561	(10)
UCAC2 16305530	M4.5	β Pic	1.58	(10)
RX J0506.2+0439	M3.8	β Pic	1.52	(10)
UCAC2 35242146	M4.0	β Pic	1.58	(10)
UCAC3 66-407600	M3.6	β Pic	1.51	(10)
HD 181327	F6V	β Pic	0.46	(2)
HD 35850	F8V(n)k:	β Pic	0.537	(2)
HIP 10679	G2V	β Pic	0.59	(1)
HIP 10680	F5V	β Pic	0.49	(1)
HIP 11437	K7V	β Pic	1.18	(1)

Notes. Stellar $B - V$ values and references are for stars in the AB Dor, Tuc/Hor, and β Pic moving groups, whose sources for Li EW did not include $B - V$ values. AB Dor and Tuc/Hor stars are from Mentuch et al. (2008), and β Pic stars are from Mentuch et al. (2008) and Shkolnik et al. (2017). Note that a single $B - V$ reference is for both B and V magnitudes, while two references are for B magnitude and V magnitude respectively.

References. (1) Mermilliod 1987; (2) Høg et al. 2000; (3) Monet et al. 2003; (4) Torres et al. 2006; (5) Riaz et al. 2006; (6) Messina et al. 2010; (7) Koen et al. 2010; (8) Kiss et al. 2011; (9) Kiraga 2012; (10) Zacharias et al. 2012.

⁷ <http://www.pas.rochester.edu/~emamajek/images/li.jpg>

ORCID iDs

S. Adam Stanford-Moore  <https://orcid.org/0000-0002-0689-2607>
 Eric L. Nielsen  <https://orcid.org/0000-0001-6975-9056>
 Robert J. De Rosa  <https://orcid.org/0000-0002-4918-0247>
 Bruce Macintosh  <https://orcid.org/0000-0003-1212-7538>
 Ian Czekala  <https://orcid.org/0000-0002-1483-8811>

References

- Allard, F. 2014, in IAU Symp. 299, Exploring the Formation and Evolution of Planetary Systems, ed. M. Booth, B. C. Matthews, & J. R. Graham (Cambridge: Cambridge Univ. Press), 271
- Anthony-Twarog, B. J., Deliyannis, C. P., Harmer, D., et al. 2018, *AJ*, 156, 37
- Arriagada, P. 2011, *ApJ*, 734, 70
- Asiain, R., Figueras, F., Torra, J., & Chen, B. 1999, *A&A*, 341, 427
- Astropy Collaboration, Robitaille, T. P., Tollerud, E. J., et al. 2013, *A&A*, 558, A33
- Balachandran, S. 1995, *ApJ*, 446, 203
- Balachandran, S. C., Mallik, S. V., & Lambert, D. L. 2011, *MNRAS*, 410, 2526
- Baliunas, S. L., & Vaughan, A. H. 1985, *ARA&A*, 23, 379
- Baraffe, I., Homeier, D., Allard, F., & Chabrier, G. 2015, *A&A*, 577, A42
- Barnes, S. A. 2009, in IAU Symp. 258, The Ages of Stars, ed. E. E. Mamajek, D. R. Soderblom, & R. F. G. Wyse (Cambridge: Cambridge Univ. Press), 345
- Barrado y Navascués, D., Stauffer, J. R., Hartmann, L., & Balachandran, S. C. 1997, *ApJ*, 475, 313
- Barrado y Navascués, D., Stauffer, J. R., & Jayawardhana, R. 2004, *ApJ*, 614, 386
- Beichman, C., Barrado, D., Belikov, R., et al. 2019, *BAAS*, 51, 58
- Bell, C. P. M., Mamajek, E. E., & Naylor, T. 2015, *MNRAS*, 454, 593
- Boesgaard, A. M., & Tripicco, M. J. 1986, *ApJL*, 302, L49
- Bonfils, X., Delfosse, X., Udry, S., et al. 2013, *A&A*, 549, A109
- Boro Saikia, S., Marvin, C. J., Jeffers, S. V., et al. 2018, *A&A*, 616, A108
- Bowler, B. P. 2016, *PASP*, 128, 102001
- Brandt, T. D., & Huang, C. X. 2015, *ApJ*, 807, 58
- Brandt, T. D., Kuzuhara, M., McElwain, M. W., et al. 2014a, *ApJ*, 786, 1
- Brandt, T. D., McElwain, M. W., Turner, E. L., et al. 2014b, *ApJ*, 794, 159
- Burke, C. J., Pinsonneault, M. H., & Sills, A. 2004, *ApJ*, 604, 272
- Casagrande, L., Schönrich, R., Asplund, M., et al. 2011, *A&A*, 530, A138
- Chiang, E. I., & Murray, N. 2002, *ApJ*, 576, 473
- Choi, J., Dotter, A., Conroy, C., et al. 2016, *ApJ*, 823, 102
- Cummings, J. D., & Kalirai, J. S. 2018, *AJ*, 156, 165
- Cunha, M. S., Aerts, C., Christensen-Dalsgaard, J., et al. 2007, *A&ARv*, 14, 217
- Cutri, R. M., Skrutskie, M. F., van Dyk, S., et al. 2003, *yCat*, 2246, 0
- David, T. J., & Hillenbrand, L. A. 2015, *ApJ*, 804, 146
- de Zeeuw, P. T., Hoogerwerf, R., de Bruijne, J. H. J., Brown, A. G. A., & Blaauw, A. 1999, *AJ*, 117, 354
- Delorme, P., Schmidt, T., Bonnefoy, M., et al. 2017, *A&A*, 608, A79
- Donahue, R. A. 1993, PhD thesis, New Mexico State Univ.
- Duncan, D. K., Vaughan, A. H., Wilson, O. C., et al. 1991, *ApJS*, 76, 383
- Fanson, J., McCarthy, P. J., Bernstein, R., et al. 2018, *Proc. SPIE*, 10700, 1070012
- Ford, A., Jeffries, R. D., James, D. J., & Barnes, J. R. 2001, *A&A*, 369, 871
- Ford, E. B., & Rasio, F. A. 2008, *ApJ*, 686, 621
- Frelikh, R., Jang, H., Murray-Clay, R. A., & Petrovich, C. 2019, *ApJ*, 884, 47
- Gallet, F., & Bouvier, J. 2013, *A&A*, 556, A36
- Giampapa, M. S., Hall, J. C., Radick, R. R., & Baliunas, S. L. 2006, *ApJ*, 651, 444
- Gossage, S., Conroy, C., Dotter, A., et al. 2018, *ApJ*, 863, 67
- Goudfrooij, P., Girardi, L., Kozhurina-Platais, V., et al. 2014, *ApJ*, 797, 35
- Gray, R. O., Corbally, C. J., Garrison, R. F., et al. 2006, *AJ*, 132, 161
- Guillout, P., Kluttsch, A., Frasca, A., et al. 2009, *A&A*, 504, 829
- Hall, J. C., Henry, G. W., Lockwood, G. W., Skiff, B. A., & Saar, S. H. 2009, *AJ*, 138, 312
- Henry, T. J., Soderblom, D. R., Donahue, R. A., & Baliunas, S. L. 1996, *AJ*, 111, 439
- Høg, E., Fabricius, C., Makarov, V. V., et al. 2000, *A&A*, 355, L27
- Isaacson, H., & Fischer, D. 2010, *ApJ*, 725, 875
- Jenkins, J. S., Jones, H. R. A., Tinney, C. G., et al. 2006, *MNRAS*, 372, 163
- Jones, B. F., Fischer, D., Shetrone, M., & Soderblom, D. R. 1997, *AJ*, 114, 352
- Jones, B. F., Fischer, D., & Soderblom, D. R. 1999, *AJ*, 117, 330
- Keenan, P. C., & McNeil, R. C. 1989, *ApJS*, 71, 245
- King, J. R. 1998, *AJ*, 116, 254
- King, J. R., & Schuler, S. C. 2005, *PASP*, 117, 911
- King, J. R., Villarreal, A. R., Soderblom, D. R., Gulliver, A. F., & Adelman, S. J. 2003, *AJ*, 125, 1980
- Kiraga, M. 2012, *AcA*, 62, 67
- Kiss, L. L., Moór, A., Szalai, T., et al. 2011, *MNRAS*, 411, 117
- Koen, C., Kilkeny, D., van Wyk, F., & Marang, F. 2010, *MNRAS*, 403, 1949
- Konopacky, Q. M., Rameau, J., Duchêne, G., et al. 2016, *ApJL*, 829, L4
- Kraft, R. P. 1967, *ApJ*, 150, 551
- Lachaume, R., Dominik, C., Lanz, T., & Habing, H. J. 1999, *A&A*, 348, 897
- Lovis, C., Dumusque, X., Santos, N. C., et al. 2011, arXiv:1107.5325
- Macintosh, B., Chilcote, J. K., Bailey, V. P., et al. 2018, *Proc. SPIE*, 10703, 107030K
- Makarov, V. V. 2006, *AJ*, 131, 2967
- Mamajek, E. E. 2012, *ApJL*, 754, L20
- Mamajek, E. E., & Hillenbrand, L. A. 2008, *ApJ*, 687, 1264
- Mamajek, E. E., Meyer, M. R., & Liebert, J. 2002, *AJ*, 124, 1670
- Meibom, S., Mathieu, R. D., Stassun, K. G., Liebesny, P., & Saar, S. H. 2011, *ApJ*, 733, 115
- Mentuch, E., Brandeker, A., van Kerkwijk, M. H., Jayawardhana, R., & Hauschildt, P. H. 2008, *ApJ*, 689, 1127
- Mermilliod, J. C. 1987, *A&AS*, 71, 413
- Mesa, D., Baudino, J. L., Charnay, B., et al. 2018, *A&A*, 612, A92
- Messina, S., Desidera, S., Turatto, M., Lanzafame, A. C., & Guinan, E. F. 2010, *A&A*, 520, A15
- Milli, J., Higon, P., Christiaens, V., et al. 2017, *A&A*, 597, L2
- Monet, D. G., Levine, S. E., Canzian, B., et al. 2003, *AJ*, 125, 984
- Nielsen, E. L., & Close, L. M. 2010, *ApJ*, 717, 878
- Nielsen, E. L., de Rosa, R. J., Macintosh, B., et al. 2019, *AJ*, 158, 13
- Nielsen, E. L., Liu, M. C., Wahhaj, Z., et al. 2013, *ApJ*, 776, 4
- Noyes, R. W., Hartmann, L. W., Baliunas, S. L., Duncan, D. K., & Vaughan, A. H. 1984, *ApJ*, 279, 763
- Pace, G. 2013, *A&A*, 551, L8
- Pace, G., Castro, M., Melendez, M., Theado, S., & do Nascimento, J.-D., Jr. 2012, *yCat*, 541, A150
- Pecaut, M. J., & Mamajek, E. E. 2013, *ApJS*, 208, 9
- Pecaut, M. J., & Mamajek, E. E. 2016, *MNRAS*, 461, 794
- Perryman, M., Hartman, J., Bakos, G. Á., & Lindgren, L. 2014, *ApJ*, 797, 14
- Randich, S., Pallavicini, R., Meola, G., Stauffer, J. R., & Balachandran, S. C. 2001, *yCat*, 372, 868
- Randich, S., Tognelli, E., Jackson, R., et al. 2018, *A&A*, 612, A99
- Riaz, B., Gizis, J. E., & Harvin, J. 2006, *AJ*, 132, 866
- Sestito, P., & Randich, S. 2005, *A&A*, 442, 615
- Shkolnik, E. L., Allers, K. N., Kraus, A. L., Liu, M. C., & Flagg, L. 2017, *AJ*, 154, 69
- Simard, L., Ellerbroek, B., Bhatia, R., Radovan, M., & Chisholm, E. 2016, *Proc. SPIE*, 9908, 99081V
- Skumanich, A. 1971, *BAAS*, 3, 455
- Snaith, O., Haywood, M., di Matteo, P., et al. 2015, *A&A*, 578, A87
- Soderblom, D. R. 2010, *ARA&A*, 48, 581
- Soderblom, D. R., Duncan, D. K., & Johnson, D. R. H. 1991, *ApJ*, 375, 722
- Soderblom, D. R., Jones, B. F., Balachandran, S., et al. 1993, *AJ*, 106, 1059
- Soderblom, D. R., Oey, M. S., Johnson, D. R. H., & Stone, R. P. S. 1990, *AJ*, 99, 595
- Sung, H., & Bessell, M. S. 1999, *MNRAS*, 306, 361
- Talon, S., & Charbonnel, C. 2010, in IAU Symp. 268, Light Elements in the Universe, ed. C. Charbonnel et al. (Cambridge: Cambridge Univ. Press), 365
- Tamai, R., Cirasuolo, M., González, J. C., Koehler, B., & Tuti, M. 2016, *Proc. SPIE*, 9906, 99060W
- Tobin, J. J., Hartmann, L., Fűrész, G., Hsu, W.-H., & Mateo, M. 2015, *AJ*, 149, 119
- Torres, C. A. O., Quast, G. R., da Silva, L., et al. 2006, *A&A*, 460, 695
- Turner, D. G. 2012, *AN*, 333, 174
- VandenBerg, D. A., & Stetson, P. B. 2004, *PASP*, 116, 997
- Virtanen, P., Gommers, R., Oliphant, T. E., et al. 2020, *NatMe*, 17, 261
- Weber, E. J., & Davis, L., Jr. 1967, *ApJ*, 148, 217
- Wright, J. T., Marcy, G. W., Butler, R. P., & Vogt, S. S. 2004, *ApJS*, 152, 261
- Zacharias, N., Finch, C. T., Girard, T. M., et al. 2012, *yCat*, 1322, 0
- Zapatero Osorio, M. R., Béjar, V. J. S., Pavlenko, Y., et al. 2002, *A&A*, 384, 937